The Effect of Compressive Residual Stresses on the Properties of Tumbled-Processed Cemented Carbide

by

Eugene Michel Keown

Thesis submitted in fulfilment for the degree of Master of Science by Research

School of Metallurgy and Materials
College of Engineering and Physical Sciences
University of Birmingham

September 2016

Abstract

For cemented carbide, classified as a brittle material, very little plastic deformation will occur preceding the initiation of a crack and ultimate failure, hence the yield strength and rupture strength are essentially identical. It is well known that compressive residual stress (CRS) helps to counteract the inherent brittle nature of cemented carbide. CRS is of benefit as it helps prevent crack growth. It is commonly applied via a post sintering treatment process on parts like mining inserts. The purpose of this research is to gain a deeper understanding of the benefits high compressive residual stresses bring to cemented carbide and how it manifests within the matrix material. By focusing on rock drill inserts, the development of a new inventive acoustic tumbling method will be discussed. This method can significantly increase the depth of CRS up to 6 mm and by utilising this method, the benefits that the increased CRS has on the mechanical properties of the material will be presented.

WC- Co composites with 11wt% Co and a mean tungsten carbide grain size of 4 micrometres were treated at different accelerations. The hardness, toughness and compressive strength were measured. Discreet element modelling was used to describe the process and mechanics of the treatment method in order to define the optimum processing parameters. Complementary techniques like EBSD, TEM and XRD were used to examine the effect of compressive stresses on the WC and Co. A significant increase in coercivity (Hc) was recorded in the treated samples and this could be directly related to the kinetic energy applied to the system.

In samples exposed to treatment at 40G acceleration, compressive stresses were measured as deep as 6mm. In compressive strength tests, these samples showed an increase of 61% of the compressive strength. These samples have the maximum

hardness increase of approximately 100 HV30 close to the treated surface. No Palmqvist cracks could be observed even at HV100. EBSD analysis showed no correlation between the Hc increase and grain refinement due to the treatment process. TEM and XRD revealed a large number of dislocations in the WC phase and Cobalt phase. It is plausible that these dislocations interact with each other and forming tangles resulting in the strengthening of the material. This project has highlighted the significant benefits of CRS in cemented carbide where by it increases the plasticity and reduces the tendency to brittle fracture failure. Thus opening up the range of applications cemented carbide can be used in the future.

Attestation

I understand the nature of plagiarism, and I am aware of the University's policy on this.

I certify that this dissertation reports original work by me during my University project

Signature: Eugene Keown **Date 15/10/2017**

Acknowledgements

Firstly, I would like to acknowledge my employer Sandvik for the financial support and the opportunity given to me to combine this project work with a postgraduate research degree. I would like to thank, Prof. Chuan-Yu Wu and Dr. Chunlei Pei for conducting the discreet element modelling, Ohio State University for the transmission electron microscopy images, Dr. Joan Josep Roa for conducting the micro-pillar testing and Jessica Marshall for conducting the EBSD analysis. I would like to thank my supervisor Dr Yu-Lung Chiu for his advice and superb support guiding me through the challenging phases. Finally, I would like to thank my wife Victoria for all her encouragement and moral support, helping me to stay the course.

Table of Contents

List of Figures

List of Tables

1 Introduction

1.1 Background

Carbide plays an indispensable part in the mining industry where it is a commonly used material in several important components from drilling bits (Figure 1) to general wear parts [1]. The inserts of the drilling bits need to have a high wear resistance during the removal of the brittle rock but at the same time high toughness in order to withstand the impact generated by the drilling action. During the drilling action the inserts hit the rock at rates of 50 times per second with hydraulic impact pressure of about 170 – 200 bar while the percussive or rotary drill head which the inserts are attached to, rotates at 75 –200 rpm [2]. The demand on tool performance pertaining to the insert material and its resistance to wear and fracturing becomes more critical for harder rock and mineral formations.

A B

Figure 1. Example of two types of drill bits consisting of a steel cylinder with Cemented Carbide (CC) inserts, protruding from the drill bit front; A) Rotary tri cone drill bit, B) Rotary percussive drill bit.

Drill heads are specifically designed for the type of drilling and the rock formation it will encounter. For example, rotary percussive drilling is used for very hard rock, such as quartzite or granite. The insert shape also plays a vital role in the performance of the

bit and a large variety of shapes exists to maximise the rate of penetration in specific rock formations. Sculptured inserts are used in roller cone bits where high penetration rates are required in soft rock. Hemispheric button inserts is normally spherical or ballistic, and used in both roller cone drills and percussive hammer bits where extra strength is required [3]. The various shapes can be seen in figure 2 below.

Figure 2. Example of different cemented carbide inserts.

Cemented tungsten carbide (CWC) is perfectly suited to operate in these extreme environments, due mainly to its unique properties. Tungsten carbide (WC) grains provide the resistance to wear with the relatively ductile cobalt, cementing the grains together, and thus providing good fracture toughness. CWC with various compositions (also known as grades) are produced with the properties tailored to fit specific bit designs and drilling conditions. The overall performance can be adapted to suit the application by adjusting the composition and microstructure of the material. For example, a combination of a low binder content and a small WC grain size offer high hardness and could be used in applications where wear is an important factor but this is at the expense of toughness and therefore prone to fracture. On the other hand high binder content and an increased WC grain size is a combination that focuses on the toughness but not hardness and consequently has a shorter life when exposed to wear [4]. Never-

theless, the typical failure mechanisms encountered in drilling applications is attributed to surface cracking which is caused by the lack of impact toughness. When the critical crack size is reached, the insert will suffer catastrophic failure under a particular application loading condition. Most drilling applications requires a high toughness and therefore the most common cemented carbides used in rock drilling tools contain 5-12 wt.% Co and 88-95 wt.% WC with its grain size in the range of 1-6 μm [5]. The common failure mechanisms that the CWC inserts are exposed to include wear, spalling, corrosion, thermal fatigue and surface cracking [6].

Wear of the carbide insert is normally caused by hard abrasive minerals in the rock formation being drilled. The soft binder phase is removed during the service and the WC grains are exposed, causing them to fall out. Wear is considered the common mechanism of degradation because no breakages have occurred allowing for full use of the insert geometry.

Spalling is generally experienced in inserts with high hardness and low toughness. It is caused by small cracks forming at the surface of the material through such mechanisms as excessive cold working that is followed by relief of the accumulated strain energy by means of crack growth towards the surface. The lack of toughness allows the crack to propagate freely resulting in various size flakes or chips.

Corrosion damage often refers to the selective attack to the cobalt binder by the service environment and the WC grains are then left to fallout. The process repeats itself leading to premature insert failure.

Thermal fatigue is observable in all types of mining. It is a distinctive bi-axial or crosshatched pattern consisting of cracks intersecting at right angles. These cracks are formed due to rapid cooling of the hot insert surface caused due to long contact exposure against the rock being drilled. It is the friction between the two surfaces that

generates the heat. These thermal fatigue cracks are caused by high stresses that arise due to the great difference in thermal expansion coefficients between the WC grains and the cobalt binder phase [7]. The cracks can become stable at a depth of 0.25 mm to 2.5 mm below the surface, and the total stability of the insert then becomes a function of the material's ability to withstand further crack propagation, known as toughness (K_{1C}).

Surface cracking, as mentioned before, is the most common cause of insert failure generated at areas experiencing high compressive loading. These small cracks grow to a critical size through intermittent high loading or fatigue failure. By using a material with a higher K_{1C}, the crack would be more stable and less likely to propagate.

It can be seen from the above that it is important to have the insert material with high K_{1C} and high hardness. The relationship between the toughness and the hardness is often as shown in Figure 3 [8, 9].

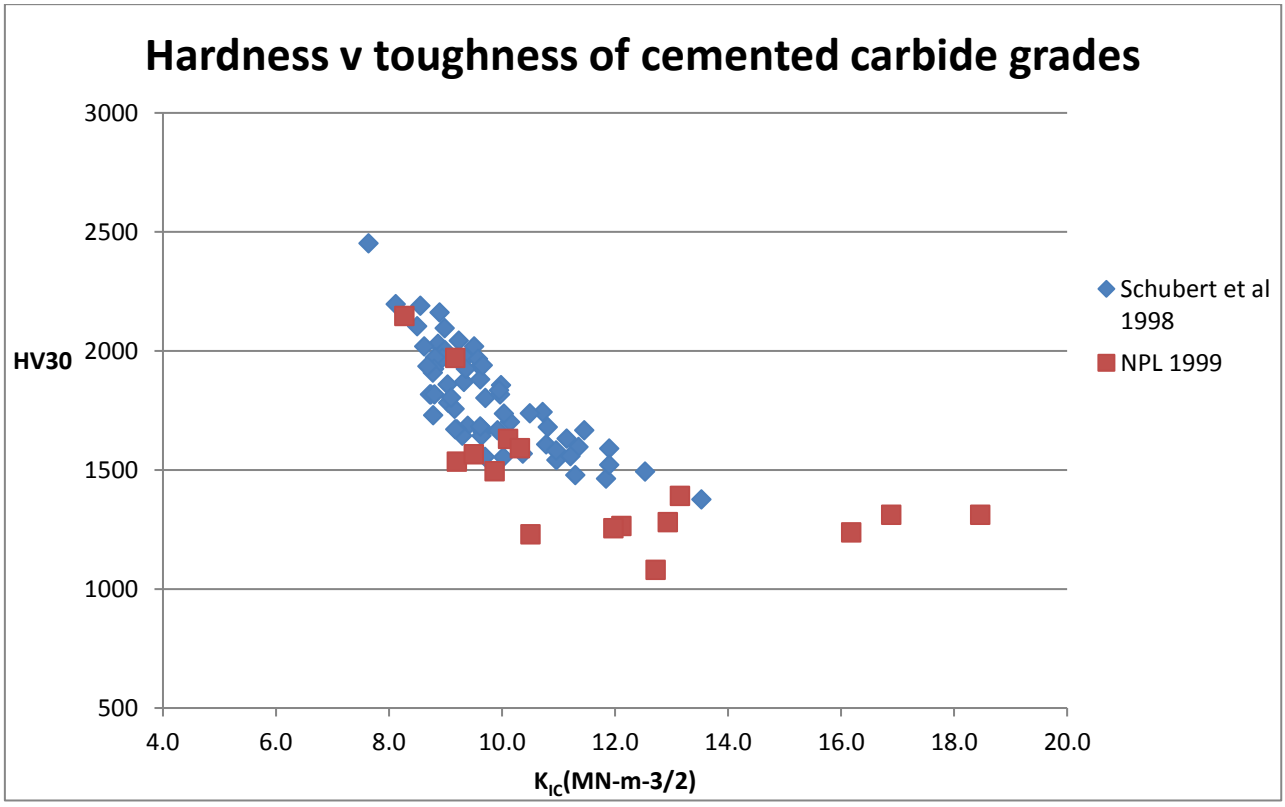

Figure 3. Hardness v toughness of various cemented carbide grades.

Another cause of early failure can be attributed to the binder tensile stress. The tensile stress developed during the cooling from the liquid phase sintering due to different thermal expansion coefficients between the carbides and binder phase [10]. As an example, these undesirable residual stresses in the Co phase have been estimated at about 1850 MPa at room temperature in equilibrium with WC [11]. As the carbide is hammered against the rock during service, small cracks occur in the carbide insert surface; these micro-cracks can easily propagate through the material that is under tension resulting in early catastrophic failure and a dramatic reduction in tool life. Residual stress plays a vital part when it comes to crack propagation in cemented carbide. Introducing a small amount of compressive stress into the surface of the insert could effectively overcome this. Different methods have been developed through the years to introduce compressive stress into mining inserts to increase the K_{1C} [12, 13].

Traditionally a post sintering surface treatment is applied to inserts through for example vibration tumbling, centrifugal tumbling or shot peening. These known surface hardening treatments are based on mechanical impact or deformation of the outer surface of the body. Shot peening is a common procedure to improve the static and cyclic strength of metal components. The process imparts a combination of work hardening and compressive stress into the surface region of the material and significantly increases the near-surface strength [14]. This method is mostly used in welded joints or edge strengthening and is sometimes used on tungsten carbide when surface finish is not a major requirement. One limiting factor of this method though is the excessively long processing time when treating large amounts of small parts like inserts.

Another process to improve the strength and life of inserts involves tumbling the inserts in a vibration tumbler. This process is better suited to handle a larger volume of parts in which the inserts constantly make contact with tumbling media and one anoth-

er causing work hardening or strain hardening that results in a strengthening of the material by means of low temperature plastic deformation, the same mechanism seen in shot peening. Though beneficial, the depth of compressive residual stress is in order of Micrometres due mainly to the limited amount of velocity and/or energy generated in this method [15].

1.2 Objectives and overview

Even though post tumbling of drilling inserts is used as a standard production step, the physical change on the cemented carbide microstructure that occurs from the application of compressive residual stress is not very well studied. Sandvik is one of the world's leading suppliers of machines and tool systems for all rock surface and mineral excavation. It invests heavily in the research and development of new grades and methods of improving the working life of the products in their portfolio. A recent development in relation to mining inserts led to an invention of a new method, capable of increasing the depth of compressive residual stress from micrometres to millimetres, giving rise to an opportunity to study the effects on the microstructure and how this relates to the performance.

The aims of this study are:

- To investigate the effect of inducing very high compressive residual stresses in cemented carbides, on the microstructural changes and on the fracture toughness in relation to crack initiation.
- To understand the mechanics of the treatment method utilizing discreet element modelling.

- To show how the magnetic domains change due to the influence of the treatment on the metallic binder system, and how it is a useful tool to correlate the level of compressive stress and increase in performance.
- To show the clear benefits of high compressive residual stresses and strain hardening in cemented carbide.

2 Literature Review

2.1 Cemented Carbide

The unique properties of cemented carbides originate from its structure. It is a metal matrix composite with a hard carbide phase as the main component set in a metal binder. The ductile nature of the metal binder serves to offset the characteristic brittle carbide ceramic, therefore raising the toughness and durability of the composite. A typical example of cemented carbide is tungsten carbide with cobalt as the binder as shown in figure 4, this is the material system used in this research project.

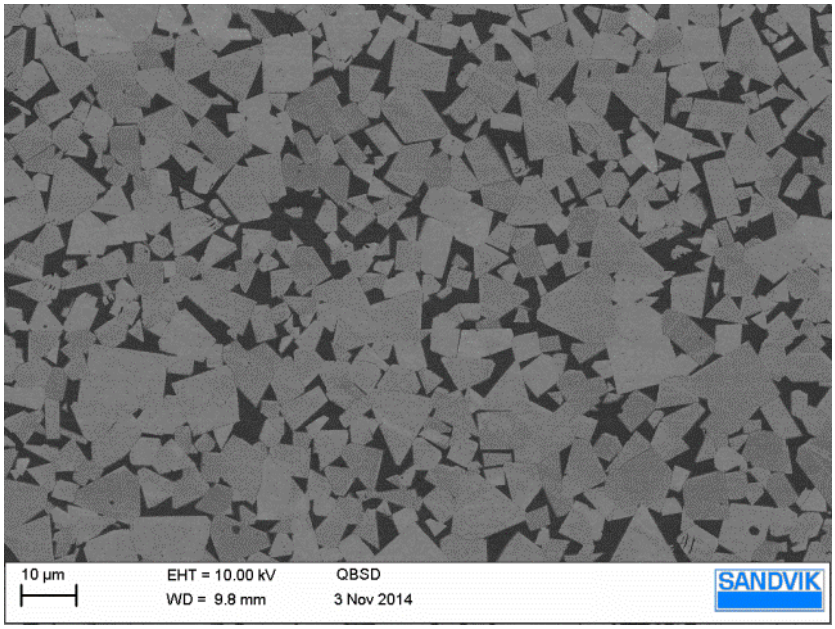

Figure 4. An SEM micrograph showing the microstructure of tungsten carbide using cobalt as the binder.

Although the history of cemented carbide can be traced back to 1896 when Moissan produced the first tungsten carbide W2C, it was not until 1925 that Schröter, at Osram Studiengesellschaft, combined it with cobalt in search of a better wire-drawing die [16]. The addition of cobalt to tungsten carbide not only allowed the sintering of dense compacts at reasonable temperatures, but also resulted in materials with adequate toughness with very high hardness. The Krupp Company went on to market with a

composition of WC and 6 % cobalt binder, called Widia [17]. Future developments of Schroter's compositions led to a major discovery in 1929. By replacing a weight percentage of tungsten carbide with other carbides (in particular those titanium or, tantalum based), it was shown that small additions of these carbides were essential for cutting steel at high speeds [18]. This discovery that a combination of carbides was superior to individual carbide led to the development of multi-carbide cutting tools for high speed machining [19]. The requirement on hardness and toughness remains central to the design of modern tool materials.

The properties of cemented carbide depend on its composition (e.g. carbon content and different carbide additions) and microstructure (e.g. grain size). For instance, low binder content and small WC grain sizes renders high hardness and wear resistance. This however could lead to low toughness and therefore prone to fracture during application. A high binder content and an increase in WC grain size work oppositely. Figure 5 shows a range of products with different combinations of WC grain size and cobalt content.

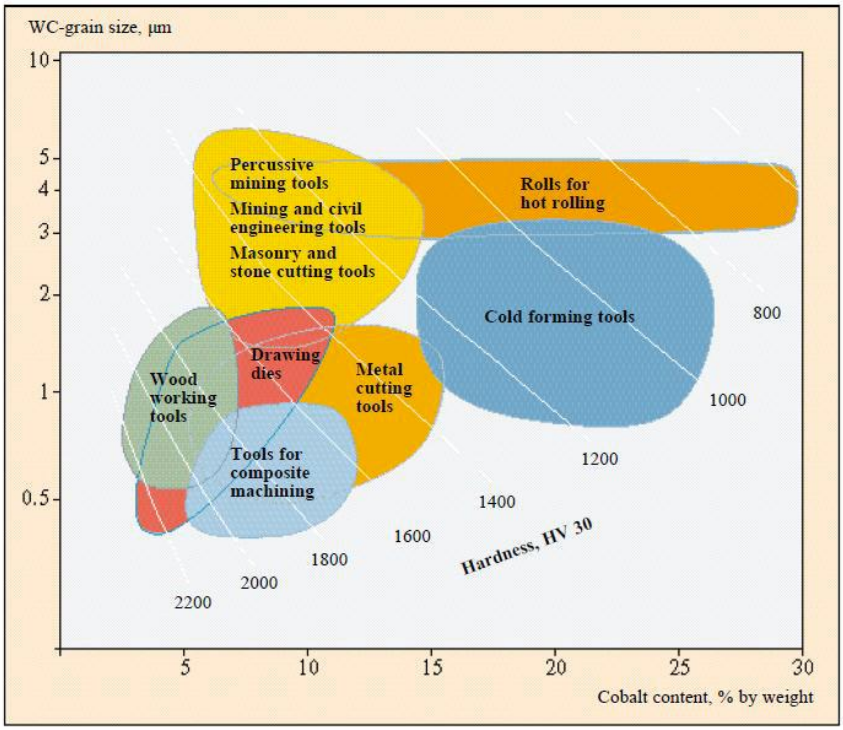

Figure 5. WC grain size and cobalt content in relation to products

2.1.1 Tungsten Carbide (WC)

Tungsten metal is extracted from two primary sources. The first is Wolframite, an iron manganese tungstate mineral, (Fe, Mn)WO_4, which comes from the German words "*wolf rahm*", the name given to tungsten(W) by Johan Gottschalk Wallerius in 1747 [20]. The other, Scheelite is a calcium tungstate mineral with the chemical formula $CaWO_4$. The Scheelite ore is treated with hydrochloric acid, which produces tungstic acid (H_2WO_3) and calcium chloride when heated. After a washing and filtering procedure ammonia (NH_3) is added to the tungstic acid in order to form ammonium tungstate. It then undergoes an evaporation process that forms Ammonium Para Tungstate (APT) crystals. The APT is then calcined in either an oxygen bearing atmosphere between 560°C to 850°C to form WO_3, a yellow oxide, or in a vacuum above 450 °C that forms a mixture of WO_3 and WO_2, a blue oxide. The oxides can

then be reduced within a hydrogen atmosphere at high temperature to form tungsten metal.

The next phase in the production of WC is mixing tungsten metal with carbon and heating it to temperatures of 1400 -1800 °C under a hydrogen atmosphere to produce WC [21]. The control of the carbon additions is of importance as too high a carbon content can lead to the formation of graphite in the hardmetal whereas too little can lead to the formation of η-phase a brittle (W, Co)6C composition. Both formations have a detrimental effect on the life of the hardmetal. The WC, also known as the α-phase, forms the hard phase of the cemented carbide and usually makes up 85 to 97 wt% of the composite. It has a hexagonal close packed (HCP) structure with a strong anisotropic surface energy that results in a prismatic crystal structure after sintering, with tungsten in position (0,0,0) and carbon in position (⅓,⅔,½) or, equivalently, (⅔,⅓,½) [22], see figure 6.

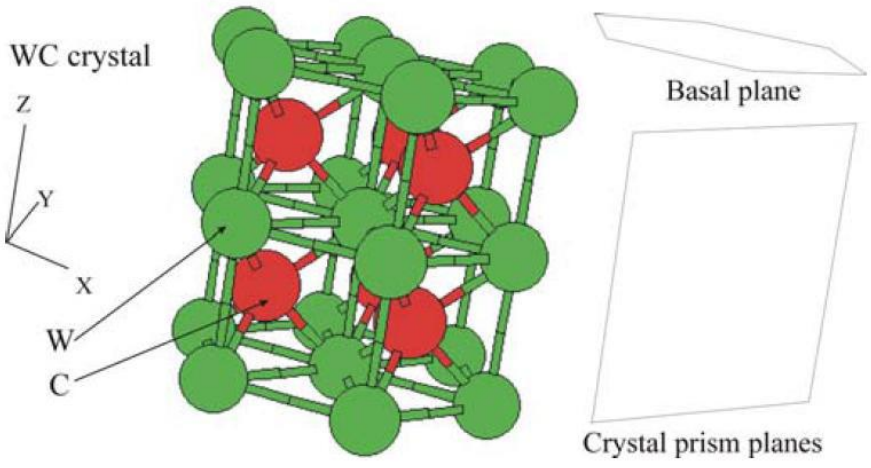

Figure 6. Crystal structure of hexagonal WC and indications of crystal prism- and basal planes.

2.1.2 Cobalt

The usage of cobalt as a colouring for glass can be traced back as far as 2250 BC but it was only in the early 20th century that the first cobalt alloys, known as Stellites came on the market [23]. These days the cobalt metal powder used in powder metallurgy and specifically in cemented carbide is usually produced through pyrolysis under hydrogen at about 550 °C of a cobalt salt, like cobalt oxalate. The latter is made by reacting oxalic acid and cobalt chloride [24]. Cobalt's low interface energy and the strong covalent CO-C bonds when used with WC, allows for exceptional wettability [25]. This cobalt binder phase, or β-phase, acts as the cement that binds the WC grains. As it is more ductile in comparison to WC, it allows for some plastic deformation before formation of cracks and fracture. The reason why cobalt has been the dominant binder system in cemented carbide as appose to others like nickel or iron is that it fulfils all the criteria required to make good performing cemented carbide while other metals only fulfil some. These consist of a high melting point; adequate high temperature strength; liquid phase at a manageable temperature of approximately 1275°C; The ability to dissolve WC by forming a eutectic with the hard phase between 1275°C and 1350°C; The ability to maintain W in the binder phase when cooled; the ability to be ground down into fine grains of < 1μm that aids with mixing and resultant sintered microstructure

Pure Co transforms from a hexagonal close packed (hcp) phase into a face centred cubic (fcc) structure at 418 °C and starts to melt at 1495 °C [26]. During sintering Co readily dissolves W and C, and after solidification the crystallographic structure of the binder phase consist of a combination of fcc and hcp due to the W dissolution in the hardened binder [27]. After sintering the cobalt interlayers are no longer pure cobalt, they exist as a solid solution of tungsten and carbon atoms in cobalt (γ-phase) due to the partial dissolution of the tungsten carbide. The physical properties of the γ-phase are shifted away from the properties of pure cobalt, and completely depend on the quantity of dissolved W [28].

2.2 Production of cemented carbides

The manufacturing process begins with a milling process were the composition of a specific tungsten carbide powder mixture is tailored for the application. The spray dried tungsten carbide powder is compacted into a form. The tungsten carbide powder is compacted into a form. In a high-temperature sintering furnace, the tungsten carbide is sintered precise temperatures for strictly defined periods. During this heat treatment, the tungsten carbide form undergoes shrinkage of some 50% in volume. The sintered Cemented Carbide component gains its final finish by additional grinding, lapping and/or polishing processes. Figure 7 shows the process of the cemented carbide production at Sandvik.

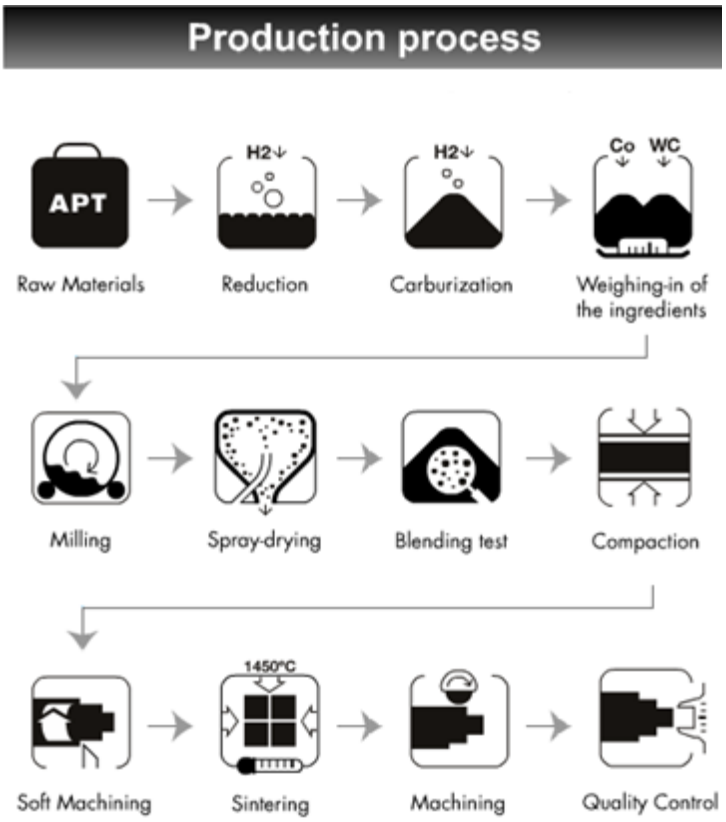

Figure 7 Example of production method employed by Sandvik [29].

2.2.1 Milling

Raw materials (powders) are mixed together in a rotating mill along with small cemented carbides also known as cylpebs. The purpose of the cylpebs is to break down the WC agglomerates and to promote thorough cobalt dispersion. The powder is milled in alcohol (+ 10% water) and a pressing aid like polyethylene-glycol (PEG) or wax is added. The PEG is added in a solid state and does not dissolve in the alcohol hence the need for the 10% water addition to dissolve it into the mix. This combination creates a viscous mix that aids the milling process. The milling time is related to the final size of the WC grains. The milling time ranges from two to 10 hours for extra coarse grain size and up to 40 ~ 60 hours for sub-micrometre grain size. Alcohol is used to reduce the risk of oxides forming and to aid in the spray drying process due to the low temperature needed for evaporation. After milling, the slurry is spray dried in nitrogen gas to form spherical agglomerates between 50 and 200 micrometre in size. Nitrogen is used due to the lower energies needed to evaporate. The spray dried powder is ready to press (RTP). The RTP powder has a uniform density that results in consistent granule crushing strength that aids compaction.

2.2.2 Powder compaction

The RTP powder is pressed under an external pressure to form a compact (green body). There are many processes to achieve this: die pressing, extrusion, cold iso-static pressing (CIP), dry bag pressing, powder injection moulding (PIM) etc. Die pressing in the simplest form, consists of a feed shoe that delivers the powder into a die cavity with an upper punch and lower punch delivering the pressure. The bottom punch is usually static. As the top punch travels downwards, the powder is packed together into a more compacted state at first. As the punch continues, the powder granules undergo

plastic deformation to form a dense compact. The top punch retracts and the bottom punch moves the compact up and out of the die cavity. Uniaxial pressing has its limitations when it comes to pressing complex geometries, due to a density gradient in the green body that causes distortion in the sintering process. The disadvantages have been eliminated by countless advances in machinery, using floating dies, upper and bottom die travel during compaction, and well-designed die and punch orientations [30].

2.2.3 Sintering

The sintering profile has three important stages;

The first step in the sintering process is to remove the organic binder. The furnace temperature is steadily increased to 450 °C, with the ramp rate defined by the size of the part. If the ramp rate is too steep when sintering a large compact, the removal of the PEG would be too fast and this would cause the compact to crack. Between 250 °C and 450°C H_2 gas is introduced to help with the removal of the PEG. The PEG molecules decompose to gaseous products such as CO, H_2O, CO_2, CH_4, alcohols etc. and evacuated from the furnace [31].

The next stage is a fast temperature ramp in vacuum, eliminating impurities. Oxides left over from the milling process will go through a reduction reaction with carbon as the reducing agent forming gaseous non-metallic oxides, CO_2 and CO. The reaction products are then pumped away. During this stage, the compact experiences some solid state sintering and shrinkage, which is mainly due to a porosity level of about 25 vol. % [32]. The reduction of total surface energy is the dominant driving force during this stage of sintering. The porosity gives rise to a high total surface energy and since the free surfaces of the particles represent a higher energy than internal boundaries, i.e. grain boundaries, the system lowers its total energy by converting the free surfaces to

grain boundaries and eliminating pores by vacancy migration to the surface. A high percentage of total shrink age occurs during this solid stage sintering.

The final stage is the top temperature needed to consolidate the compact. This can range between 1300°C and 1450°C and requires the compact to stay at the set temperature for a set amount of time to insure it reaches its maximum density. This melting and or solidification temperature is influenced by the grade composition but usually the isotherm is 1 hour long. At this point, the metal binder (e.g. Co) is in a liquid phase since it has reached the eutectic temperature in the system. The amount of C in the system plays a vital role at the amount of cobalt in the liquid state at different temperatures, which can be seen in the phase diagram in Figure 8. The Carbon level in the system also influences the W/WC in solid solution. Using Classical sintering theory, this liquid phase is divided into three steps [33]:

1. Rearrangement is the first process step. As the liquid binder wets the solid phase, due to a decrease in surface energy, capillary forces are generated which pulls the particles together causing a decrease in porosity and increase in density. This rearrangement under viscous flow of the liquid and the pace at what it occurs at overshadows the opposing frictional force generated between the solid particles [34, 35].

2. As densification by rearrangement slows, the solution precipitation process becomes dominant. Due to compressive stress in the contact points between the WC particles, a higher chemical potential is generated. A solution of the solid phase of the material is transported away from the contact points through the liquid and re-precipitated on surfaces with the lower chemical potential. During this stage, densification is accompanied by considerable coarsening (grain growth) and by grain shape changes

3. When the Ostwald ripening process becomes dominant, the third step of Coalescence begins. Grains of dissimilar size start to fuse into a single grain by grain growth, rotation or grain reshaping. This leads to decrease in grain numbers and results in grain coarsening, which is directly related to the temperature and time spent in liquid phase.

Usually when sintering sub-micrometre grades, Argon gas is pumped in to create high pressures > 30 bar, this helps to close micro pores and helps the compact reach maximum density. This is also known as hot isostatic pressing (HIP).

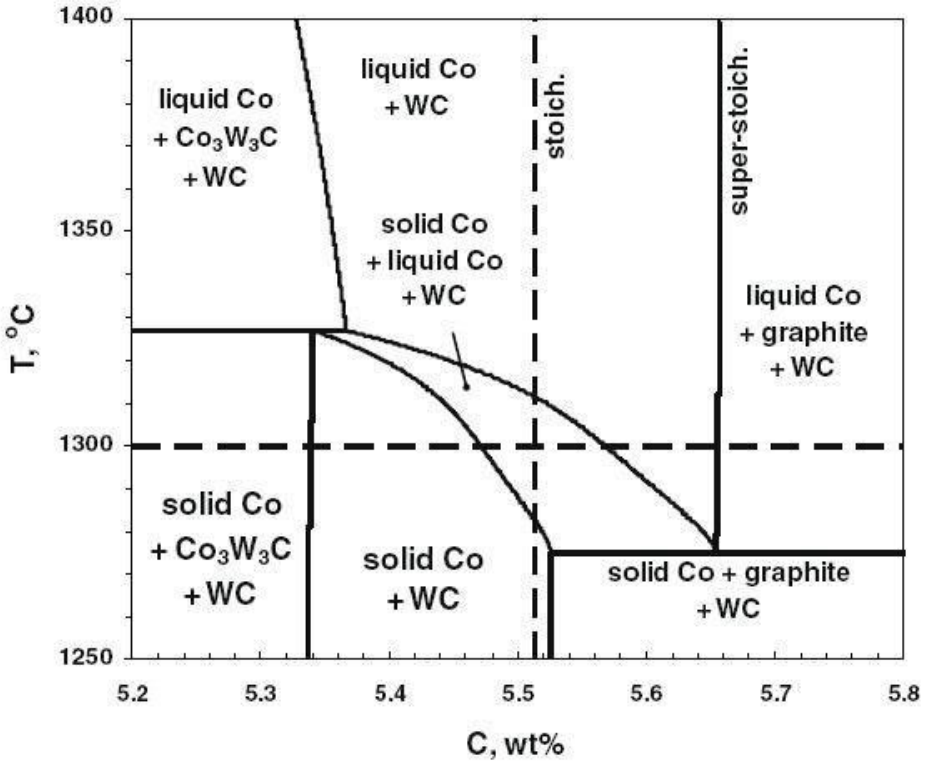

Figure 8. A cross-section of the ternary W-Co-C phase diagram at 10 wt.% Co. The liquid phase sintering is carried out in a temperature where the Co is in liquid state [36].

2.2.4 Machining

After sintering, the parts undergo some form of finishing step depending on the application requirements and dimensional tolerances needed. Due to the hardness of the cemented carbide, this process is important to be kept at a minimum due to the cost and time involved. These requirement drives research in order to improve near net shape manufacturing. Different methods consist of machining and or grinding with some parts undergoing a further surface treatment.

2.3 Current methods of imparting surface residual stress

The surface of a sintered cemented carbide part is often treated by a surface hardening method to improve the mechanical properties of the body. Traditionally this surface treatment is applied to drill bits for example through vibration tumbling, centrifugal tumbling or shot peening. Another example of a surface treatment method is cascading [37]. These known surface hardening treatments are based on mechanical impact or deformation of the surface layer of the body, such that a work hardening zone forms at and just below the surface. It is known that cold working is beneficial due to the plastic deformation changing the grain shape, increasing the dislocation density and increasing the strain energy of the crystal lattice [38].

2.3.1 Shot peening

Shot peening is a cold working method that utilizes high velocity spherical particles to impact the surface of the material being treated. During peening, the highly localized blows deform and tend to stretch the metal surface. This surface deformation is countered by the material underneath, producing a compressive residual stress in the

surface. Since the compressive stresses subtract from existing or applied tensile loads, they tend to add fracture resistance to the product [39]. The effectiveness of the process is controlled by the velocity, size and composition of the impacting material [40].

2.3.2 Tumbling

Tumbling is the standard method used for imparting residual stresses into the mining inserts. Samples simply hit each other and the container wall. This method is mainly used for polishing, cleaning and deburring of varied material but due to the movement, the collisions invariably causes some plastic deformation leading to residual stresses imparted into the samples. Sandvik predominately uses this method to impart CRS for their products. A range of different tumbling equipment exist to achieve the desired effect. In vibrational tumbling, the inserts are loaded into a vibrating bowel or circular container. The amplitude and frequency of the vibrations can vary and the vibrations are three dimensional. The parts are subjected to a consistently high frequency tilting movement as they travel in a helical/orbital path around the chamber. The resulting compressive scrubbing and impact action imparts the compressive stresses. In horizontal drum tumbling, the inserts rotating in the drum and are lifted up by the walls until they fall down under gravity on top of other inserts. The amount of samples and the speed the drum rotates at are important parameters that affect the result Centrifugal barrel tumbling is similar to drum tumbling except that the barrel is attached to the end of a rotating arm. The addition of centrifugal force to the weight of the parts in the barrel makes the process faster than conventional drum tumbling.

2.4 Coercivity

Since cobalt is ferromagnetic, the W-Co alloys display magnetic properties despite a considerable content of the non-ferromagnetic WC-phase. These measured characteristics are closely associated with the structural parameters of the cobalt interlayer, and makes it possible to use as a non-destructive test for quality inspection of the sintered products. Coercivity measurement is readily used in quality control as an indication of the average sintered WC grain size present in the sample. This Hc value is the size of the reversed magnetic field needed to de-magnetise a fully magnetised sample. When Cemented carbide has compressive residual stress due to some form of post mechanical treatment e.g. tumbling, the Hc value increases by small margins. This increase is depended on the kinetic energy of the tumbling process. Understanding the reason for using Hc (Coercivity) as a measurement tool and what it reveals about the material with compressive residual stress, it is needed to understand the mechanics behind this value. An explanation on how Hc is derived follows.

Magnetic Hysteresis, the delay or lag of a magnetic material, relates to the magnetisation properties of a material by which at first, it becomes magnetised and then de-magnetised. It is known that an electromagnet depends upon the number of turns of a coil, the current flowing through the coil and the type of material being used as a core. If the current is increased or the number of turns in the coil is increased we can increase the magnetic field strength. This is donated by the symbol H. In addition, the flux density given by the symbol B is the amount of magnetic field lines produced within a given area.

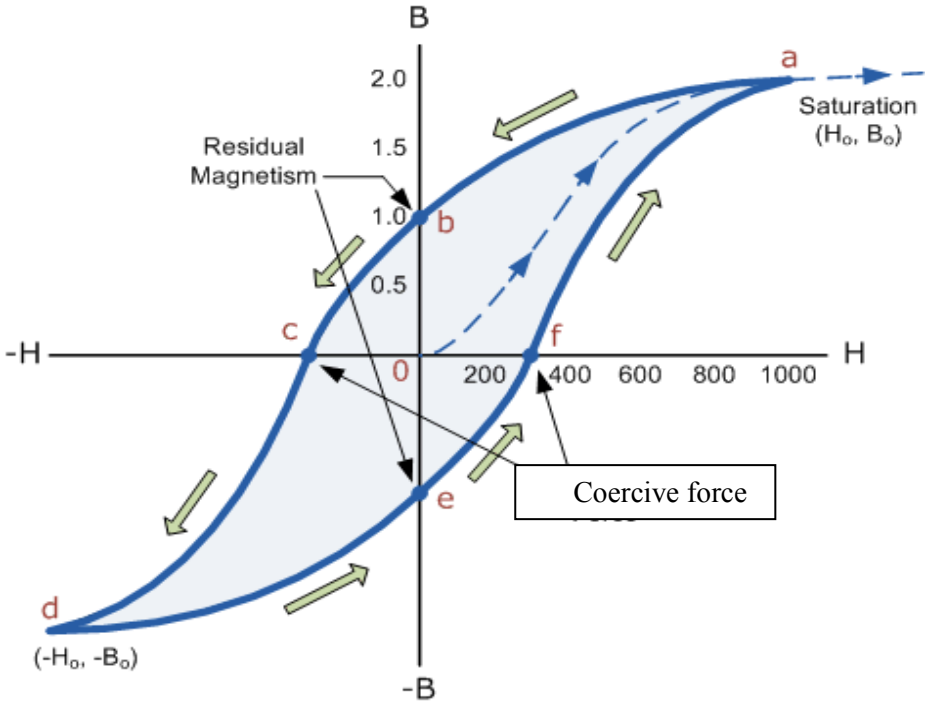

Figure 9. Example of the hysteresis curve, showing the points on the curve relating to the coercive force

Some primary magnetic properties one can determine from the hysteresis loop are as follows:

1. ***"Retentivity*** *– this is a measure of the residual flux density corresponding to the saturation induction of a magnetic material. It is the material's ability to retain a certain amount of residual magnetic field when the magnetizing force is removed after achieving saturation. (The value of B at point b on the hysteresis curve.)*
2. ***Residual Magnetism or Residual Flux*** *- the magnetic flux density that remains in a material when the magnetizing force is zero. Residual magnetism and retentivity are the same when the material has been magnetized to the saturation point. However, the level of residual magnetism may be lower than the retentivity value when the magnetizing force did not reach the saturation level.*

3. ***Coercive Force*** *- The amount of reverse magnetic field which must be applied to a magnetic material to make the magnetic flux return to zero. (The value of H at point c on the hysteresis curve.)*
4. ***Permeability, μ*** *- A property of a material that describes the ease with which a magnetic flux is established in the component.*
5. ***Reluctance*** -Magnetic reluctance is the ratio of the amplitude of the magneto-motive force (MMF) and the magnetic flux in the circuit.*"* [41]

In these test we are mainly concerned with the Coercive force, the Hc value. In cemented carbide a fine-grained grade has a higher Hc value than a coarse grained grade due to the fact that the magnetic domains in the binder phase will be harder to demagnetise because of the increase density of domain walls.

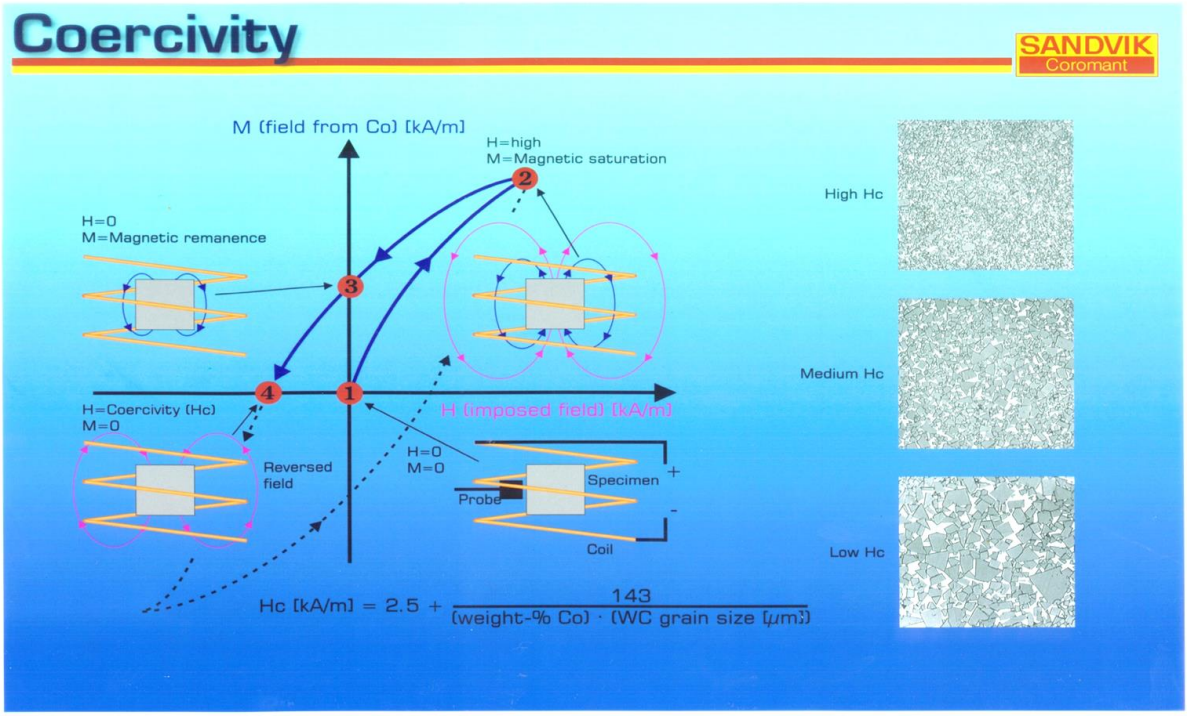

Figure 10. Overview of the hysteresis curve and microstructure in relation to high and low Hc

This variation of coercive force and the fact that it decreases as the percentage of cobalt increases and/or the grain size decreases is described by Stjernberg [42], Fisch-

meister et al [43] and Roebuck et al [44]. Another aspect that was first suggested by Becker in 1932 was the existence of inhomogeneous strain within the crystal being a dominant factor in resistance to magnetic domain wall movement also known as strain theory [45]. Both are a possible mechanism that explains the increase in Coercivity seen in cemented carbide that has CRS.

2.5 Compressive strength

Under compressive loading ductile materials will bulge or swell without fracture whereas a brittle material will fail, due mostly to a shear fracture. Cemented carbide exhibits very high compressive strength when compared to most other material. This value can be improved with compositional changes such as low binder and reduction in grain size. The determination of compressive strength of cemented carbide is a common test method, and in principle it consists of placing a dumb bell shape test piece between two hardmetal bearing blocks (anvils). The sample is then subjected to an axial load until the sample deforms or fractures [46]. In mining applications the cemented carbide grade is specifically chosen for the type of rock that needs drilling, but the shape of the part is also a factor. In softer rock formations a chisel shape is used to increase the rate of penetration and in a harder rock formation a dome shape is employed to distribute the stresses and increase the life of the tool. The compressive strength results obtained from the standard test is a good indication of the intrinsic material property but it does not take the shape of the real working part into account and how it is used in the application. This kind of data is usually obtained from real field tests but the parameters are hard to control and often the results are ambiguous.

2.6 Electron Back Scatter diffraction

Electron Back Scatter Diffraction (EBSD) is a technique where electrons fulfilling Bragg's criteria for coherent diffraction form channelling patterns (Kikuchi lines)

which can be detected with a phosphor screen. Diffraction patterns can be used to build up an image as a raster pattern, displaying different grains and phases using colour coded maps known as Orientation Image Maps (OIM). Using suitable sample preparation techniques, different phases in cemented carbides can be isolated or all phases can be imaged simultaneously. EBSD is a powerful technique which enables grain size and shape to be measured over thousands of WC grains. A significant limitation of EBSD is that it is very sensitive to sample preparation as the crystal lattices need to be relatively strain free as this distorts the lattice. Sample preparation routes for EBSD aim to eliminate the strain induced by the cutting, grinding and polishing required to produce a cross-sectional sample and provide a clean, flat surface free from scattering and contamination. EBSD works on the principle of electron diffraction which means that the specific Kikuchi patterns depend on the orientation of the diffracting crystal lattice. It is therefore possible to generate OIM where the specific orientation of each WC grain is known. The fact that different crystal phases have different lattice parameters makes it possible to discriminate between different materials so Co and WC phases can be viewed separately.

EBSD can be used to accurately measure WC grain size and grain size distribution and determine whether WC crystals are single- or polycrystalline. Strain can be calculated from OIM since the presence of strain in a crystal lattice caused distortion of the interatomic spacing. This leads to broadening of diffraction peaks relative to a strain-free sample. Intra-granular strain in crystals detected by OIM can be calculated by the degree of misfit between the detected diffraction pattern and that simulated by the acquisition software; the greater the misorientation between the measured diffraction pattern and simulation the greater the intra-granular strain. Strain is calculated using

the median grain size for the WC phase and the nominal mean free path of the Co phase given by [47]:

$$l_{Co} = d_{WC}\ \frac{V_\beta}{(1-V_\beta)}\ l_{Co} = d_{WC}\ \frac{V_\beta}{(1-V_\beta)}$$

2.7 X-ray diffraction

X-ray diffraction (XRD) is a phenomenon in which the atoms of a crystal, by virtue of their uniform spacing, cause an interference pattern of the waves present in an incident beam of X rays. By measuring the intensity and angles of the outgoing, diffracted beams, a mapping over the different crystalline elements and lattice structure in the sample can be created.

X-ray diffraction can also be used to measure the residual stress. This is done by measuring the distance between the crystallographic planes (d-spacing) (Bragg's law), combined with Hooke's law one can calculate the stress. If a stress is applied to the crystals, the d-spacing will change resulting in a measurable shift of the peaks in the XRD spectrum and according to Hooke's law: $\varepsilon = E\sigma$ [48], where ε is the strain, E is the Young's modulus of the material and σ is the stress. A limitation of this method when used on CC is the shallow penetration depth. In a sample of 90 wt% WC and 10 wt% cobalt, chromium radiation has a calculated penetration depth of 4 µm but Kravitz showed that 90 % of the information comes from a depth of about 1.9 µm with approximately 50 % comes from the first 0.6 µm or shallower [49]. This limits the usefulness of this technique when investigating stress states in coarse CC grade.

3 Methodology

Current industry standard methods were used to evaluate the effect of compositional differences and/or post sintering treatments on mining inserts. These methods include hardness by Vickers indentation, toughness by Palmqvist method, Coercivity and compressive strength. All these methods combined, help to build an overview of the effects very high compressive residual stresses has on cemented carbides. By using other complimentary methods such as transmission electron microscopy and micro-pillar compression tests, further in depth analysis of the distribution of the stresses and how they manifest within the microstructure of the material will be investigated.

3.1 Material composition and manufacture

The material composition used in this investigation is a standard mining grade variant commonly used in the industry. The geometry of the mining insert is also a common shape used for drilling. Inserts of cemented carbide comprising the hard phase WC and the binder phase Co were manufactured as per standard production method within Sandvik. Powders of WC and Co were wet milled, spray dried and pressed to bodies of the shape of drill bits. The pressed bodies were gas pressure sintered in a vacuum at a temperature of 1410 °C to form a dense sample. .

Figure 11. Standard mining insert

Each body was in the form of a mining insert as shown in Figure 11. A cylindrical body with one spherical end and one flat end. The size of the body is 15 mm in height and 12 mm in diameter or width. The weight of one sample is about 25 g. The samples were ground using a centre less grinding equipment of Lidköping type CL630. This is the preferred method of grinding outer diameters of cylindrical shapes in large volume. It consists of two rotary grinding wheels with the workpiece secured in between. The composition and properties of the sample are shown in Table 1. The grain size is measured on a polished surface with the mean intercept method in accordance with ISO 4499 and the values presented in Table 1 are mean values with an uncertainty value of 10%

Table 1. Composition and properties of the variant used for analysis.

Sample	WC weight %	Co weight %	WC grain size (µm)	Hv 30	K_{IC}	H_c (kAm^{-1})
1	89	11	4	1250	24.4	8.2

In order to see if the newly developed tumbling method translates to other cemented carbide compositions a further three samples were treated and analysed for hardness and toughness only. These samples cover a range of binder volume and WC grain size as described in table 2.

Table 2. Composition and properties of the three variants used for hardness and toughness.

Sample	WC weight %	Co weight %	WC grain size (µm)	Hv 30	K_{IC}
2a	90	10	0.8	1600	10.7
2b	94	6	2	1600	10.3
2c	64	6	5	1440	11.1

3.2 Coercivity

All measurements were made using a Förster Koerzimat 1.095 with a 60mm diameter coil and reported in Hc (kAm-1). The weight of the test pieces were entered into the software and the sample is magnetised to saturation in a permanent Hallbach magnet array. The sample is then pulled out of the coil manually or pneumatically. During the retraction, the coils measure its magnetic moment and a flux meter in the electronics integrates the result. The final measurement, Hc, is the weight-specific magnetic saturation and magnetisable content as a percentage of the sample.

3.3 Method of inducing residual compressive stress

The materials were processed following a recent patent [50]. The samples reported on this project were mechanically treated in a lab scale Resodyne LabRam™ resonant acoustic mixer, with a maximum load capacity of 500 g. A number of parts were placed in a container,(to a specific fill volume) and vibrated utilizing the mechanical resonance frequency of the system, thus forming a system causing the bodies to move and collide with each other and the inside walls of the container. The parts experience very high accelerations, and therefore obtain high kinetic energies far higher than current standard methods utilizing conventional vibro or gravitational tumblers. One major benefit of using the acoustic mixer is its ability to adapt to the total mass of system and acquire a resonance frequency to keep the bodies at the acceleration level set by the controls. Acceleration limit of the equipment is 100G. For these tests the energy was adjusted such that a maximum acceleration of 20 G, 40 G or 60 G was achieved, wherein 1 G = 9.82 m/s^2. 10 WC inserts of 25g each were placed in a 250 mL polypropylene jar with a screw top lid and placed in the mixer. An “Auto” function was used to reach the resonance frequency within the interval of 58 – 68 Hz, landing on a

frequency of about 60 Hz. The time of treatment was varied as disclosed below. This method provides a surface zone with a higher level of hardness and toughness at a larger depth below the surface than prior art.

Figure 12 Labram acoustic tumbler on the right verses a standard vibrator bowel tumbler

3.3.1 Utilizing Discreet Element Modelling (DEM) to define treatment parameters

To better understand the process and mechanics of the treatment method, discreet element modelling was used. Utilising DEM it was possible to identify the parameters that has a direct influence on the effectiveness of the process to impart significant compressive residual stress. Model 1 parameters are a replication of the initial trial setup that yielded improved results. The dynamic behaviours of the particle system in a vibration container were investigated using 3D DEM. In DEM, the particles are treated as elastic spheres. The contact interactions between particles were computed based on classical contact mechanics: Hertz theory for the normal contact, and Mindlin and Deresiewicz theories for tangential interaction.

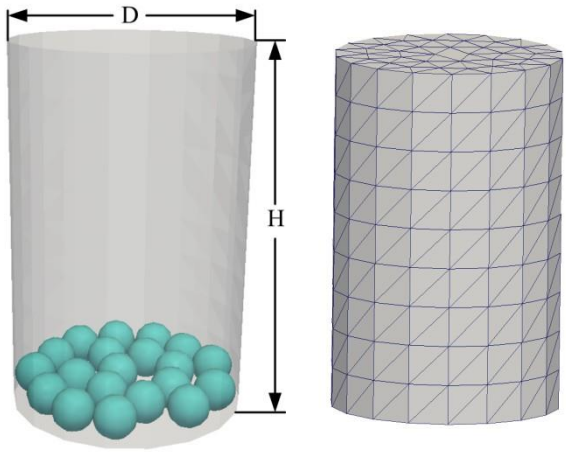

(a) (b)

Figure 13. Model Setup.

Table 3. Material properties of particles and container

	Particle	Container
Dimension (mm)	20	85 (H) × 55 (D)
Density (kg/m^3)	29.2 × 10^3	7.9 × 10^3
Young's modulus (GPa)	630	210
Poisson ratio	0.22	0.3

Table 4. Properties of contact friction and damping

Friction coefficient (P-P)	0.3
Friction coefficient (P-W)	0.3
Damping ratio (P-P)	0.016
Damping ratio (P-W)	0.032

In the model, particles were assumed to have a diameter of 10 mm and were deposited into a cylindrical container until the granular bed is settled with the maximum particle velocity smaller than 10^{-6} m·s^{-1}, as shown in Figure 13. The container then starts to vibrate and the particles in the container are agitated. In DEM, the cylindrical container is divided into triangular elements as shown in Figure 13b. During the vibration, the contact between the particle and the triangular elements were detected and calculated. The value of acceleration was set 40 G (G = 9.81 m·s^{-2}), and the frequency

(f_b) 60 Hz. Figure 14c shows the comparison between the displacement evolutions obtained from DEM analysis using the acceleration and velocity given in Figs 14a and 14b, and that obtained theoretically. It can be seen that the implemented vibration mode in DEM agrees very well with the theoretical one (Figure 14c), and the peak-to-peak amplitude is 6.8 mm. The material properties of the particles and the container are given in Table 3 and the properties of the contact friction and damping are shown in Table 4.

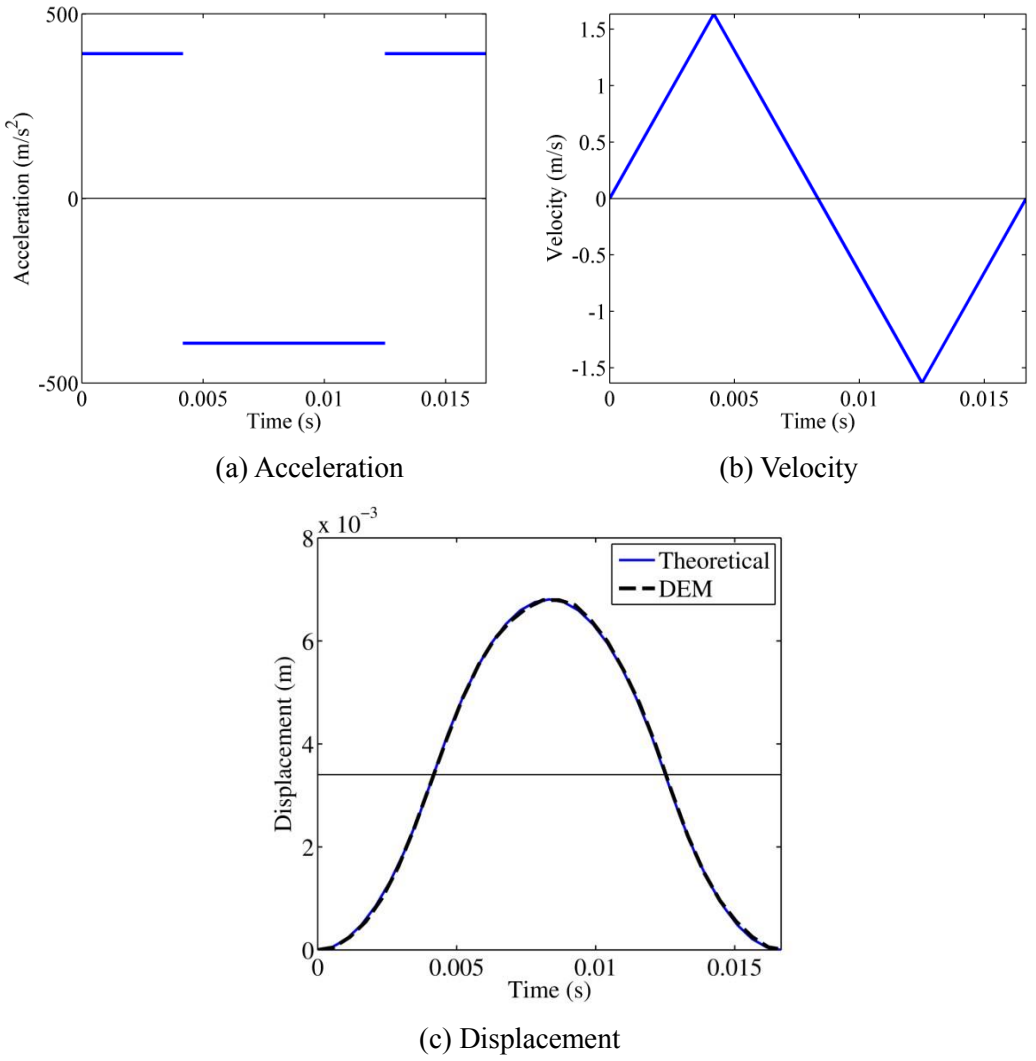

(a) Acceleration

(b) Velocity

(c) Displacement

Figure 14. The vibration mode of the model showing (a) acceleration, (b) velocity and (c) displacement.

In model 1, 20 particles were filled into the cylindrical container with H = 85 mm and D = 55 mm. The solid fraction in Table 5 is defined as the ratio between the total volume of all particles and the volume of the cylindrical container:

$$K = \frac{NV_p}{V_c}$$

Where N is the number of particles; V_p is the volume of the particle in 3D; V_C is the volume of the container in 3D. The nominal height in Table 3 is defined as:

$$h_n = \frac{NA_p}{S_c}$$

Where A_p is the cross area of the particle; S_C is the area of the cylindrical container. The nominal height can be used to approximate the number of particle layers of the granular bed without considering the porosity due to the arrangement of particles in the container as shown in Figure 13.

Table 5. Model 1 parameters dimension and number of particles

Model	H × D (mm)	Number of particles	Solid fraction	Nominal height
1	85 × 55	20	0.0519	0.66

To relate the vibration of the container with the kinetic energy evolution of the particle system, the vibration cycles of the container is defined as:

$$C_b = \frac{t}{T_B}$$

where t is the vibration time, T_b (= $1/f_b$) is the period of each vibration, which is 0.0167 s.

Key parameters examined in this study include mean kinetic energy, mean velocity and mean granular temperature.

The mean kinetic energy is defined as:

$$\tau = \langle V^2 \rangle = \frac{\sum_{i=1}^{N} V_i^2}{N}$$

where **v** is the velocity of the particle and *i* is the index of the particle. It can be seen that the kinetic energy indicates the energy level of the particle system. The mean velocity is defined as:

$$\bar{v} = \langle v_v \rangle = \frac{\sum_{i=1}^{N} v_v^i}{N}$$

where v_y is the velocity of the particle in y direction. The mean velocity indicates the average momentum of the particle system. The mean granular temperature is defined as:

$$T_g = \frac{1}{D}\langle (v - \bar{v})^2 \rangle = \frac{1}{3N}\sum_{i}^{N}\left(v_x^i - \bar{v}_x\right)^2 + \frac{1}{3N}\sum_{i}^{N}\left(v_y^i - \bar{v}_y\right)^2 + \frac{1}{3N}\sum_{i}^{N}\left(v_z^i - \bar{v}_z\right)^2$$

where *D* is the dimension of the simulation, and is 3 in this study. The granular temperature indicates the internal energy fluctuation of the particle system. A second model with varied dimensions and particles were run to test the effects in relation to kinetic energies and granular temperature, and how the process scales. The parameters used in model 2 are presented in table 6

Table 6. Model 2 with various dimensions and number of particles

Model	H × D (mm)	Number of particles	Solid fraction	Nominal height
2a	370 × 330	1000	0.0165	0.92
2b	370 × 330	350	0.0058	0.322
2c	370 × 330	720	0.0119	0.66
2d	370 × 330	1500	0.0248	1.38
2e	370 × 330	2500	0.0413	2.3
2f	370 × 330	5000	0.082	4.6

3.4 Mechanical properties test methods

Hardness and toughness were used to study and track the microstructure changes After standard tumbling and the new developed acoustic tumbling. All samples prior to any microstructural examination were mounted in Bakelite to perform a rough grinding step to remove the top sintered surface and to ensure a flat profile and good edge retention. When examining the material properties, the rough grinding step is removed when surface properties are required as to not remove too much of the induced compressive stresses. The samples are then finely ground and polished with 9 μm and then 3 μm diamond paste.This gives a good surface finish to measure the Vickers indentations by means of optical microscopy .

3.4.1 Hardness

Hardness was determined with a pyramidal diamond indenter as per ISO 3878. Hardness values for cemented carbide were measured with a 30 kg force (HV30) on a Zwick/Roell Indentec Micro & Macro Vickers Hardness tester with the load range of 1 – 120 Kgf. The Vickers Hardness (Hv) is obtained by dividing the force applied to the pyramidal diamond indenter, of 136º between opposite faces by the surface area of the impression it made in the material being tested.

$$Hv = 1.8544P/\mathrm{d}^2$$

Where:

P = Force (Kgf)

d = Diagonal of impression (mm)

A polished surface finish is required with the surface to be tested. If there was more than 4 μm difference between the diagonals of the impression, the specimen was treated as insufficiently flat for accurate determinations and the results not included.

3.4.2 Fracture Toughness

The toughness of the material was measured utilizing the Palmqvist method. This method derives fracture toughness values from measuring the total lengths of the cracks emanating from the four corners of the related Vickers hardness indent made using a load of 30 kgf (following ISO 3878 unless stated otherwise). The lengths (L) of cracks starting from the corners of the indent at were measured by optical microscope at 500× magnification. The fracture toughness of materials is determined from the critical stress intensity factor defined as K_{IC}. Palmqvist fracture toughness was assessed following Shetty et al.'s equation [51] according to:

$$\mathrm{KIc} = A\sqrt{H}\left(\frac{P}{\Sigma \mathrm{L}}\right)$$

where H is the hardness (N/mm^2), P is the applied load in Newton N, ΣL is the sum of crack lengths (mm), A is a constant of 0.0028, and $K_{I}c$ is given as MPa $m^{1/2}$ [52]. For HV30, values are expressed in (kgf/mm^2), Palmqvist fracture toughness can be calculated as [53]:

$$\mathrm{KIc} = 0.15\left(\frac{HV30}{\Sigma \mathrm{L}}\right)$$

The range of values for typical WC/Co hardmetals is from 7 to 25 MPa $m^{1/2}$ and there is a general inverse trend of hardness against fracture toughness [54]. How the crack propagates through the sample also affects the measured toughness. As an example, crack deflection due to an optimum grain size will results in increased toughness [55]. In tough mining grades, 30kg was not enough to produce consistent even cracks at 4 corners, so the load of 50 kg or 100kg was used. It is important to note that, according to the British Standard (BS ISO 28079:2009), the ability of the Palmqvist method to differentiate between materials depends on the hardness. Material with a high hardness has a low scatter.

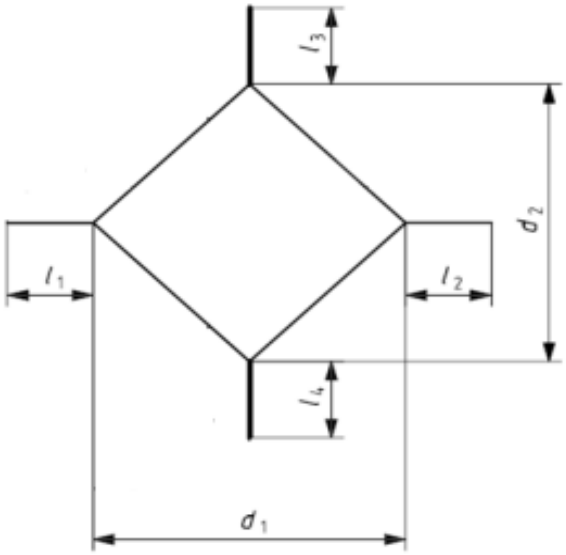

Figure 15. Diagram showing how the measurements of the Vickers indent and the corner cracks are measured.

3.4.3 Compressive strength

To see the effect of compressive residual stress on compressive strength and specifically how it relates to the mining button shape, an in house compression test method was developed with the following set up:

- Mayes mechanical tester with a 500kN load cell to record peak load at failure.

- Cemented carbide anvils on the top and bottom;
- The bottom anvil was protected by a new carbon steel shim for each test;
- The top cemented carbide anvil was replaced after every 6 tests – no shim was used on the top
- All samples tested were of the same geometry and six buttons were tested per variant.

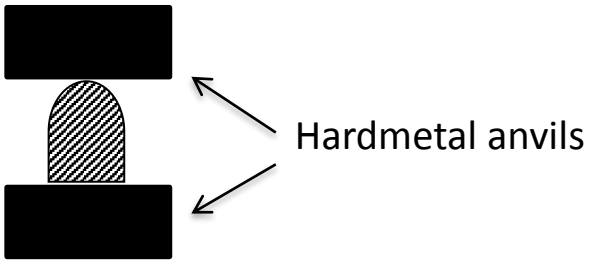

Figure 16. Diagram of compressive strength setup

3.5 Microscopy and Crystallography

3.5.1 Scanning electron microscopy

A Zeiss SUPRA 55VP FEGSEM was used for chemical composition analysis, utilizing AZtec© software. EBSD on the same microscope was used to characterise the grain refinement of the WC grains and to understand the residual strain within the binder system caused by the acoustic tumbling. Samples were sectioned using a diamond saw then wet polished using 30µm diamond laps then with 8µm, 3µm and 1µm aqueous diamond polishing media (Metprep). A final polish with 0.05µm colloidal silica (Metprep) on a neoprene lap was followed by an ion beam etch (1.8eV, ~20 µA) for 90 minute with a brief Murakami etch (20% NaOH, potassium ferrocyanide) to

remove WC profiling resulting from the polishing stage. Samples were mounted in a holder to tilt the polished face to 70º from horizontal, which is the standard set-up for EBSD analysis. OIM were produced using the Nordlys EBSD camera (Oxford Instruments). Data acquisition and processing was carried out using the Channel 5 software package. Each scan was taken at points 3 mm, 1 mm, 0.2 mm and 0.1 mm from the sample surface. Each orientation image mapping (OIM) used for grain size measurement was obtained at 30kV with a beam aperture of 120µm at a magnification of 2000, with a scan size of 500 x 400 and a pixel size of 0.2µm. Additional OIM at higher magnification were obtained at 10k magnification with a step size of 0.05µm. The following parameters extracted from the scans using the Mango module from Channel 5 were as follows: grain size (equivalent circular diameter); fcc/hcp ratio in the Co phase; strain in the WC phase and strain in the Co phase. Furthermore, a LEO MEB 35 SEM with EDX (INCA energy) was also used for imaging purpose.

3.5.2 Transmission electron microscopy

To investigate the microstructural changes of the materials at higher resolution, transmission electron microscopy (TEM) study was carried out on an FEI/Philips CM-200T microscope at the Centre for Electron Microscopy and Analysis at The Ohio State University. Sample for TEM study was prepared using a Fischione 1010 ion milling machine. TEM sample was taken from approximately 200 micrometers from the treated surface.

3.6 Micro pillar compressive strength tests

Micro pillars were machined using focused ion beam and tested on a Nanoindenter to investigate the stress-strain behaviour and associated deformation/failure mechanisms of the materials [56]. The micro pillars were prepared using a Zeiss Neon 40 FIB system operated at 5 kV. Milling process was carried out in two stages in order to minimize damage by impinging ions. Initially, a ring with outer and inner diameters of 15 μm and 4 μm was carved using an ion beam current of 4 nA. Afterwards, micro pillars with average diameter of 2 μm and an approximate aspect ratio of 2.5, were shaped using a 500 pA current. The micro pillars were uniaxially compressed using a Nano indenter XP (MTS) system fitted with a 25 μm diameter spherical punch at a constant strain rate of around 0.05 s^{-1}. Load-displacement data were continuously recorded. Nominal stresses and strains were directly determined from the load-displacements curves, using the 2 μm diameter of the pillar and its effective gauge length. Irreversible deformation and failure mechanisms have been directly examined by means of SEM system.

4 Results and Discussion

4.1 Discreet element model results.

This body of work helps to explain the treatment method and gives a good indication of the kinetic energies the particles experience, it also gives an overview of the system as a whole helping to define the parameters required to achieve the optimum results.

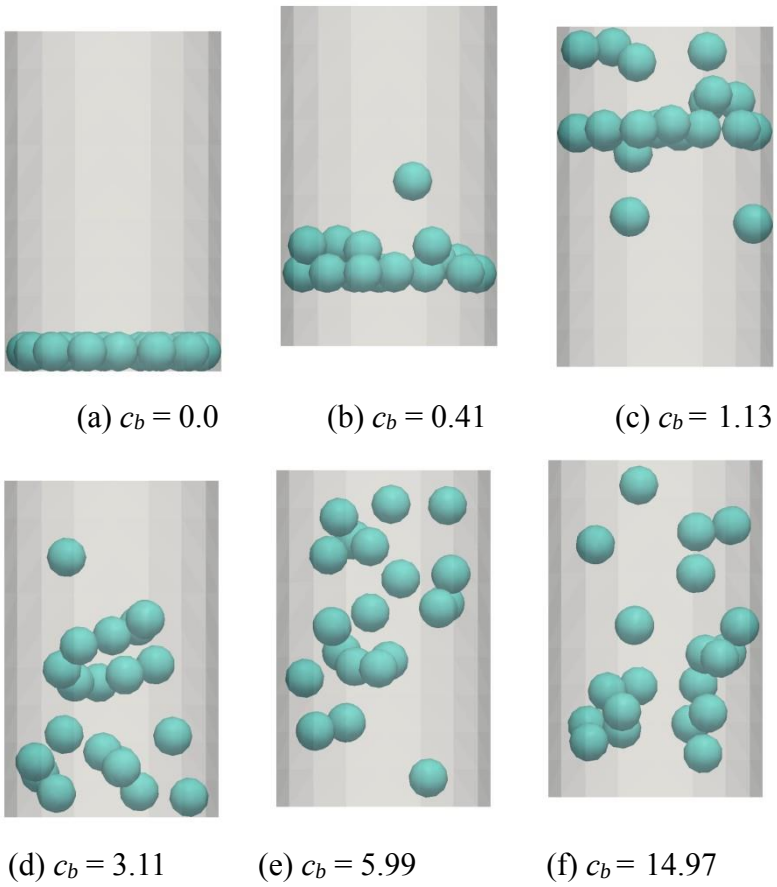

Figure 17. Particle profiles of Model 1 during vibration cycles (cb) of the container.

Figure 17 shows the particle profiles of during vibration. Particles are initially deposited at the bottom on the cylindrical container (Figure 17a). It shows there is only one layer of particles. With the vibration mode specified in Figure 13, particles are accelerated and moving upwards due to the push from the bottom wall as shown in Figure 17b. Particles continue moving until they reach the top of the container (Figure 17c) and are then bounced downwards to the bottom (Figure 17d). After a few vibrations, particles can move inside the entire container randomly (Figures 17e and 17f), due to the impact between particles and walls, especially from the top and bottom of the container.

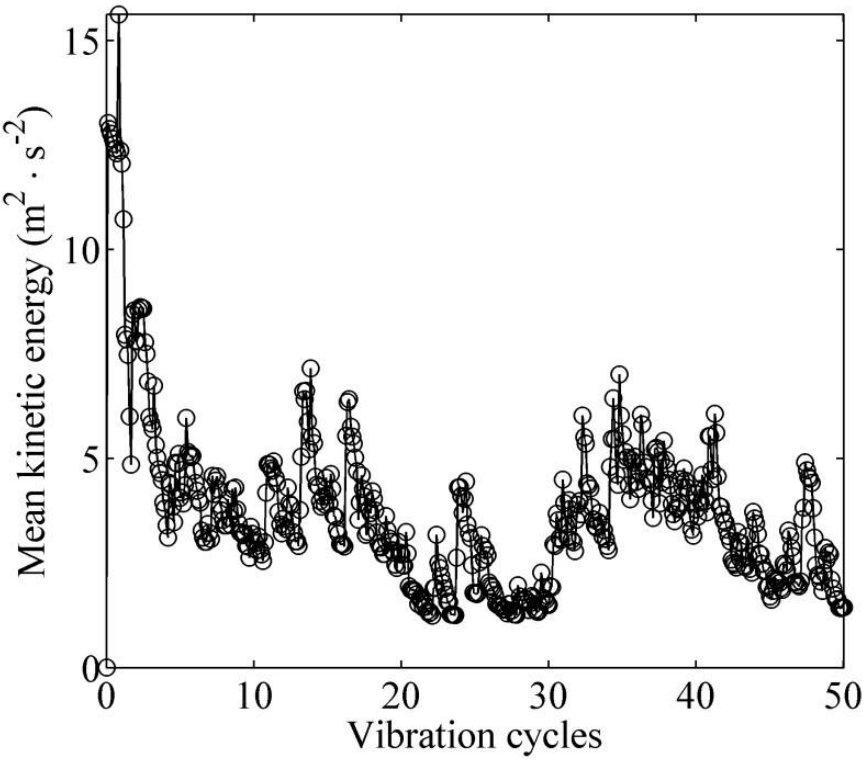

Figure 18. Mean kinetic energy mode

Figure 18 shows the mean kinetic energy of the model during vibration. Initially, the mean kinetic energy increases, because the particle system is accelerated by the container. Then the kinetic energy fluctuates as the container vibrates. The fluctuation is

caused by the impacts between particles and walls. Clearly, the impacts maintain the kinetic energy at a certain level with deviation (fluctuation). These phenomena of the mean kinetic energy correspond well with the particle movement during the vibration as observed in Figure 17.

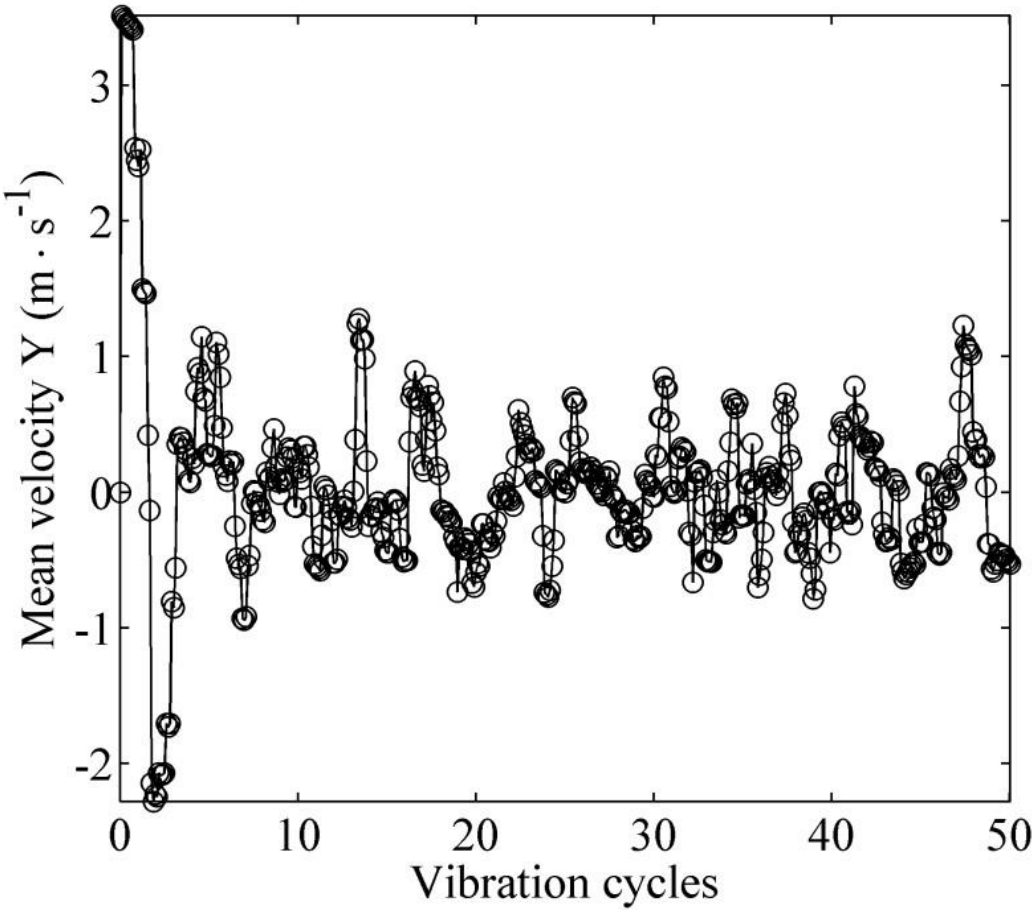

Figure 19. Mean velocity Y of Model 1.

Figure 19 presents the mean velocity of Model 1 in the Y direction during vibration. Initially, the mean velocity increases due to the upward acceleration of the particle system. Then the mean velocity decreases and becomes negative after the impact from the top wall of the container as shown in Figure 17c. As the vibration of the container continues, the mean velocity fluctuates around zero, which indicates that the particle

system moves up and down in the container. The mean velocity also reflects the movement of the particle system well, as shown in Figure 17.

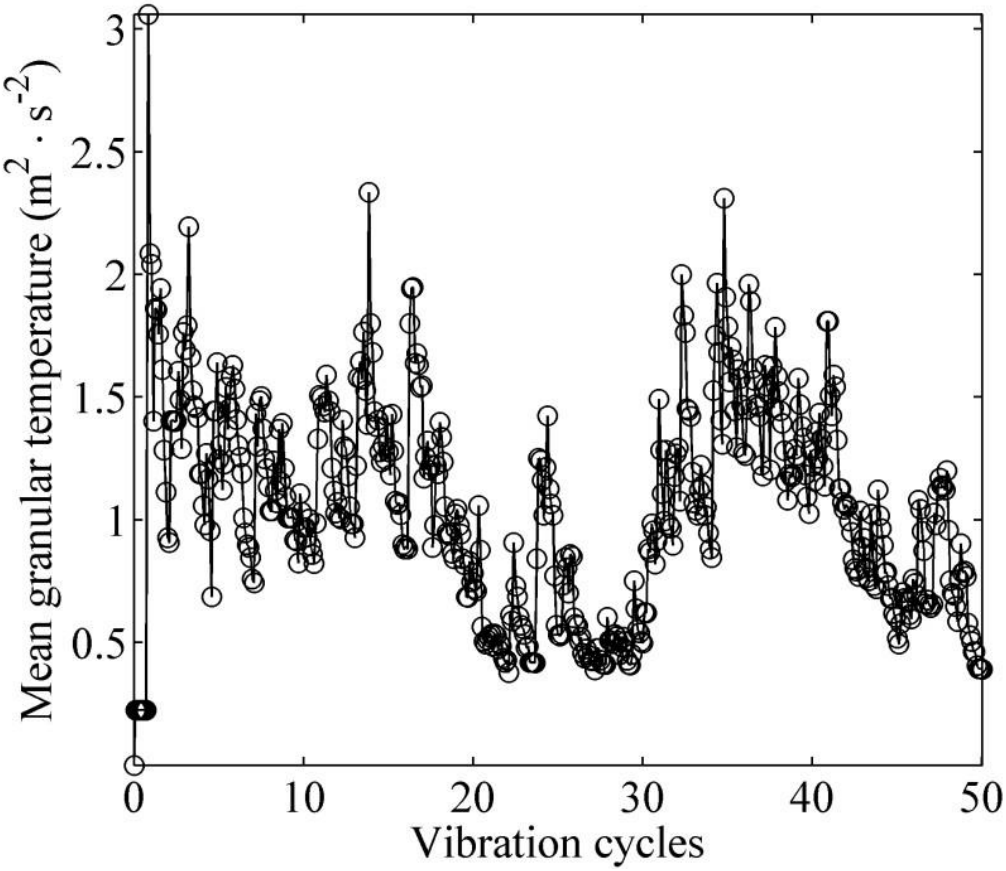

Figure 20. Mean granular temperature of Model 1.

Figure 20 shows the mean granular temperature during vibration. At the beginning of the vibration, it shows a low granular temperature. It then increases to a certain level and fluctuates with the vibration of the container. The granular temperature reflects the velocity difference between particles and the fluctuation of the internal energy. Initially, the particles at the bottom (layer) are accelerated from the push of the bottom wall. There are slight velocity differences between particles due to the impact between particles and between the particle and the bottom wall. Therefore, the granular temperature is relatively small. When all particles start to collide with each

other and with the walls, they move at different velocities and in different directions (Figures 17e and 17f). Consequently, the granular temperature fluctuates due to the velocity difference. The granular temperature shows the fluctuation of the internal energy which is different from the mean kinetic energy of the particle system, especially at the beginning stage.

It is observed that the kinetic parameters fluctuate around their overall mean values (levels) during vibration. In order to compare overall kinetic behaviours, the overall mean values of these kinetic parameters are calculated as:

$$\tau' = \frac{\sum \tau}{N_s}$$

$$v' = \frac{\sum \bar{v}}{N_s}$$

$$T_g{}' = \frac{\sum T_g}{N_s}$$

where τ', v' and Tg' are overall mean kinetic energy, overall mean velocity (Y) and overall mean granular temperature; N_S is the number of samples. In the current study, the samples are only selected from the steady fluctuation state (generally, $c_b > 20$). In addition, the sample standard deviation of these overall mean values are also determined accordingly to reflect the significance of the fluctuation.

Table 7 shows overall mean kinetic parameters of model 1. It is clear that the mean velocities fluctuate around zero, meaning particles move up and down during the vibration.

Table 7. Overall mean kinetic parameters

Model	H × D (mm)	N	Solid fraction	Nominal height	$\tau' \pm \sigma$	$v' \pm \sigma$	$T_g' \pm \sigma$
1	85 × 55	20	0.0519	0.66	3.04± 1.28	-0.025±0.39	0.94±0.40

Table 8.Overall mean kinetic parameters for model 2 with increased number of particles and varied heights

Model	H × D (mm)	N	Solid fraction	Nominal height	$\tau' \pm \sigma$	$v' \pm \sigma$	$T_g' \pm \sigma$
2a	370 × 330	1000	0.0165	0.92	3.03± 0.12	-0.021±0.091	1.01±0.042
2b	370 × 330	350	0.0058	0.322	7.02±0.43	-0.021±0.11	2.24±0.09
2c	370 × 330	720	0.0119	0.66	4.14±0.20	0.0023±0.0661	1.41±0.059
2d	370 × 330	1500	0.0248	1.38	1.80±0.085	0.043±0.04	0.60±0.027
2e	370 × 330	2500	0.0413	2.3	0.82±0.083	0.028±0.033	0.27±0.027
2f	370 × 330	5000	0.082	4.6	0.33±0.09	-0.027±0.067	0.11±0.03

In model 1 with an acceleration of 40G the kinetic energy of the system is predicted to be in the region of 3.04± 1.28 Joules with an overall mean granular temperature of 1.01± 0.042, showing good chaotic movement of the particles that result in the energetic impacts required. In model 2 the dynamic behaviours and kinetic energy vary with the number of particles and related nominal height. For models with fewer particles, the particles can move up to the top wall of the container and then down to the bottom during the entire vibration. For models with more particles, the particles only fluctuate at the bottom of the container and cannot reach the top of the container after the initial agitation. More particles in the container produce larger nominal height, which means there are more layers of particles in the container. In addition, the solid fraction will be larger for more particles in the container which can constrain the movement of particles inside the container. Therefore, for models with more particles the energy of the particle system can dissipate faster and the particles cannot move up

to the top of the container. This is recorded as a low mean granular temperature, since the majority of particles are traveling in the same direction at the same time, reducing the impact energy.

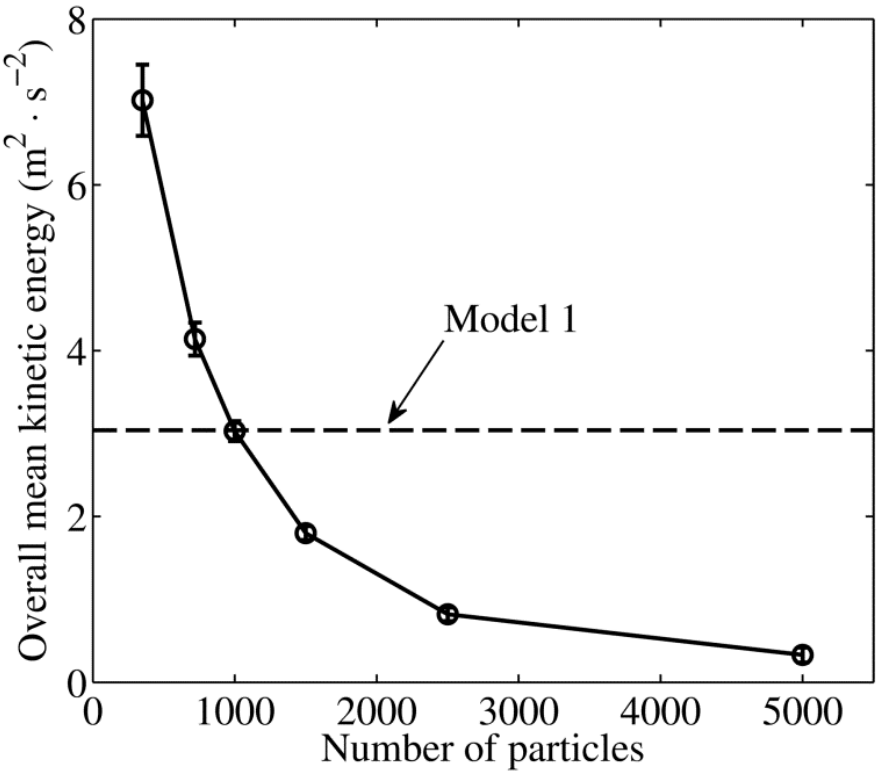

Figure 21. Overall mean kinetic energy of Models 2a – 2f.

In other words, it is difficult to gain impact energy from the wall, especially the top wall of the container to the particles system for models with more particles. The model showed that for the method to be optimum, the nominal height of the particle bed within the container should be considered. This is to allow for enough freedom between the particles in order to achieve sufficient acceleration before impact on each other. Another important factor revealed by the model is the fact that both the bottom and the top of the container needs to act on the particles. If the height of the container is too large or if the solid fraction (the amount of particles) is too high causing dampening, the system cannot obtain a steady state.

4.2 Coercivity

In the initial stages of development it was noted that the treatment has a direct influence on the coercivity of the sample. This became a useful tool to track and control the amount of treatment on the sample during the process. Sample 1 was treated at three different accelerations over the same time periods to compare the rate of Hc increase. The treatment was paused at suitable time intervals to allow measurements to be taken in order to take measurements. After treatment, a significant increase in Hc was observed. In Figure 22 we can see how the amount of acceleration and therefore potential kinetic energy effects the change in Hc over time. All samples had a starting Hc of 8.2 kA/m. After 15 minutes treatment there was a clear differentiation in Hc increase related to the acceleration. All subsequent measurements followed a similar trend. The Hc value tends to plateau around 75 minutes; at this stage the test was stopped. The total Hc increase for this time period measured as 0.48 kA/m for 20G, 1.01 kA/m for 40G and 1.56 kA/m for 60G The increase over time is related to coverage, the random collisions generated through this method require time to make sure that all the surface area has experienced impact.

Table 9. Coercivity (kA/m) as a function of the treatment time and acceleration for Sample 1

Time treated	15 min	30 min	45 min	60 min	75 min
Coercivity (kA/m) (at 20G)	8.44	8.55	8.63	8.66	8.68
Coercivity (kA/m) (at 40G)	8.66	8.84	8.97	9.09	9.21
Coercivity (kA/m) (at 60G)	9.00	9.32	9.39	9.48	9.56

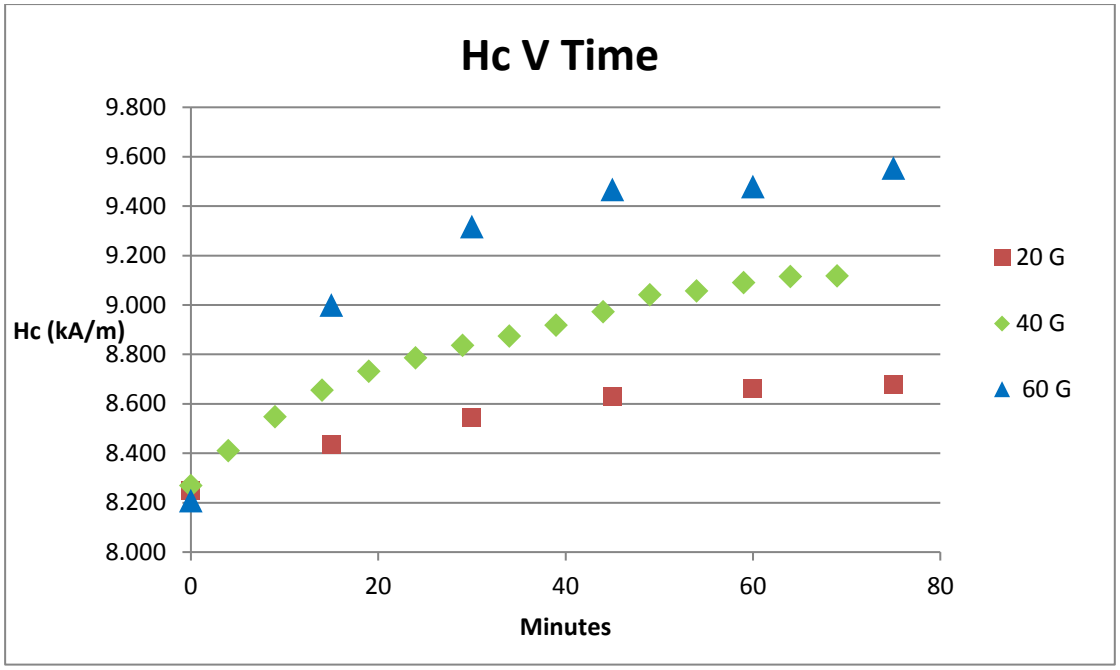

Figure 22. Increase of Coercivity over time at different accelerations

It is clear that with the increased kinetic energy the impact region extends deeper and influences the microstructure in such a way that the magnetic domains are affected and coercivity is increased. There are two possible reasons for this coercivity increase caused by the treatment method, viz.

1) Increase in the number of Weis domains in the cobalt. The coercivity value is dependent on the mobility of the Bloch walls that represents a boundary between Weis Domains, regions that are magnetised in the same direction. As the particle size of a magnetic material decreases, the number of Weiss domains increases, as does the individual leakage fields and therefore also the coercive force.
2) Increase in the number of Weis domains in the cobalt due to finer WC grains causing pinning centres within the cobalt binder. Knowing that Hc is used to infer grain size information about the hard phase, the increase in Hc indicates a possible decrease in WC grain size due to the impacts fracturing and re-embedding into the sample.

4.3 Hardness and Toughness

Hardness measurement is thought to be the most important mechanical property when it comes to choosing a grade for abrasion resistance, even though hardness alone does not dictate the success of a carbide grade in a wear application. Sample 1 was treated at 40G acceleration for 75 minutes to ensure sufficient coverage. This was based on the measured Hc value reaching a plateau and therefore indicating the complete surface of the part has been treated. The samples were sectioned and polished. Vickers hardness tests were performed on the polished section from the treated surface in to the bulk, as shown in Figure 23.

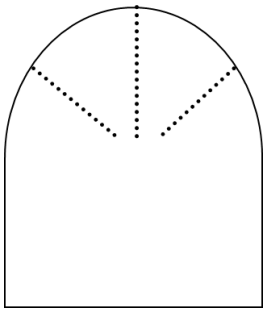

Figure 23. Schematic of HV3 Vickers indentation on treated sample to assess the depth of treatment.

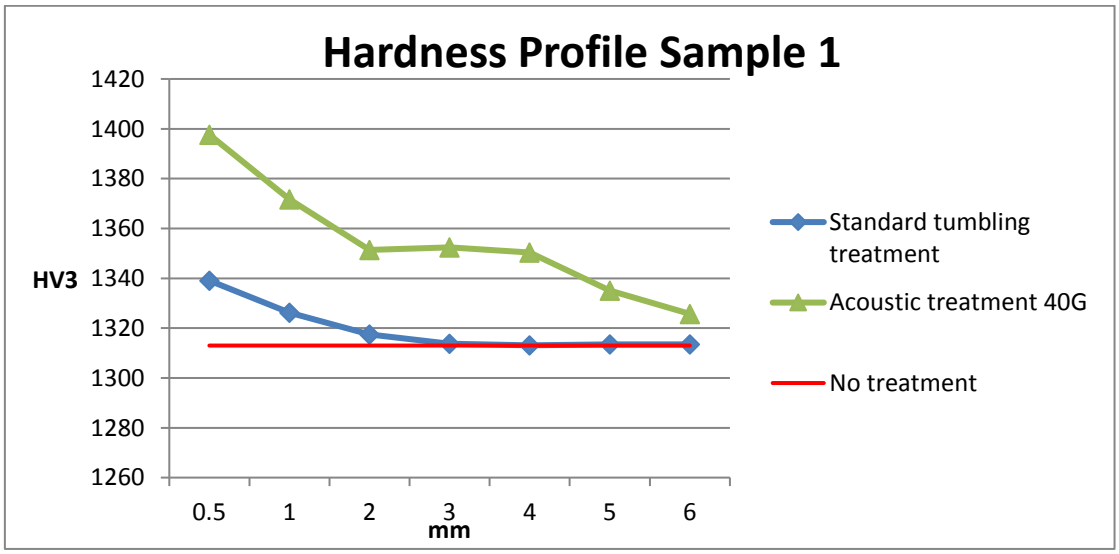

Figure 24. HV3 hardness profiles of an untreated sample, a standard tumbled sample and a 40G acoustic tumbled sample.

The material close to the surface was measured to be 100 HV harder than the unstressed control sample. Another significant result from the acoustic tumbling process is the depth of the hardness gradient. At 40G acceleration, the acoustic tumbling process has hardened the materials 6 mm into the surface, significantly deeper than that treated with standard tumbling method.

More notably was the lack of Palmqvist cracks from Vickers indentations performed close to the surface of the treated sample as shown in Figure 25. No corner crack at the indents has been observed with the applied load up to 100 kg on the treated samples. When measured with the 100 kg load, the hardness increased from 1242 HV to 1353 HV upon the treatment. The K_{IC} determined for the control sample is 24.4 MPa · $m^{1/2}$ whereas no cracks has been observed on the treated sample.

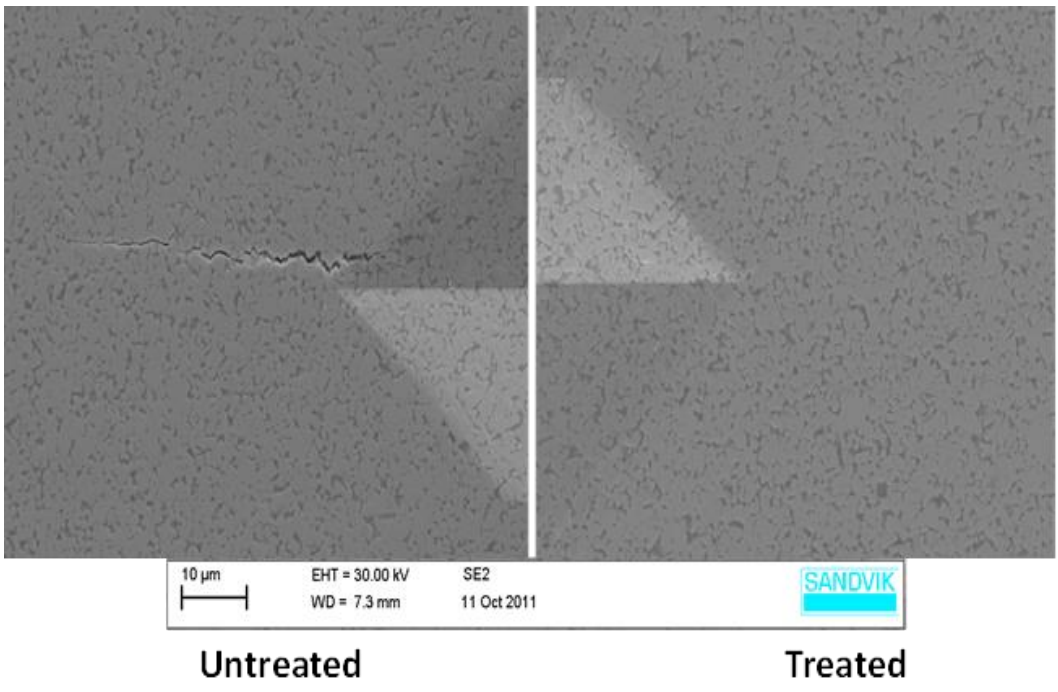

Figure 25. SEM picture of an untreated sample with the expected Palmqvist corner cracking and a treated sample with no cracks

The lengths of the cracks were measured from the indents made close to the treated surface and at the centre of the sample. The results are shown in Table 10, for the un-treated samples vis-à-vis the samples treated using the standard tumbling method and those treated with the acoustic tumbling method at 40G. While the crack length was typically 77 μm at the centre of all samples tested, the surface crack length was signif-icantly different. The acoustic tumbling treated sample shows no crack on the surface.

Table 10. Palmqvist crack length (μm)

Surface treatment	Palmqvist crack length (μm) close to treated surface	Palmqvist crack length (μm) at core
Untreated surface, as ground	77	77
Tumbling	33	77
Acoustic tumbling 40G,	0	77

Table 11 shows the effects of acoustic tumbling on two different standard carbide grades produced by Sandvik Hyperion. In each case, the fracture toughness has signif-icantly increased along with the hardness, as shown in Figure 26, moving towards the top right corner of the graph.

Table 11. Hardness and toughness of two treated samples

Sample	WC weight %	Co weight %	WC grain size (μm)	Hv 30	K_{IC}
2a	90	10	0.8	1600	10.7
2b	94	6	2	1600	10.3
2a treated	90	10	0.8	1680	19.5
2b treated	94	6	2	1689	16.8

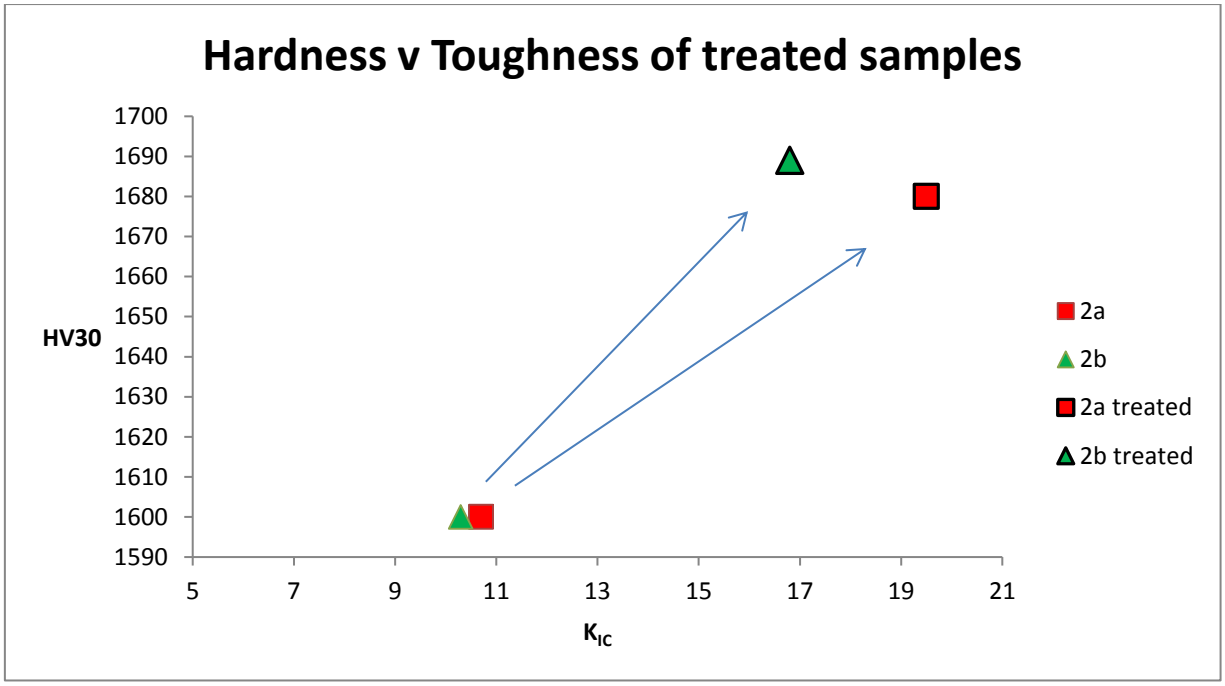

Figure 26. Increase in hardness and toughness due to the acoustic tumbling treatment

4.4 Compressive strength

Compression test results are presented in Table 12. A significant increase in resistance to failure was observed upon the treatments during the compression tests. The increase in acceleration during the treatment, as can be seen in Figure 28, leads to an increase in compressive strength. This is due to the higher kinetic energy applied which allows a larger volume of material to be treated. The untreated samples had an average failure value of approximately 83kN. Treatment at 40 G saw an increase in failure resistance of 61% to 134kN while treatment at 60G saw an increase in failure resistance of 70% to 141kN. The compressive strength test showed that the treated samples have sustained a higher amount of plastic deformation on the dome area before failure. It is also noticed that the data scatter from the tests on the treated samples

are smaller, indicating that the defect content in the sample might have been reduced by the treatment.

Table 12. Load at breakage (i.e. compressive strength)

Surface treatment	Compressive strength (kN)
Untreated surface, as ground	83.32
Invention 40 G	134.72
Invention 60 G	141.55

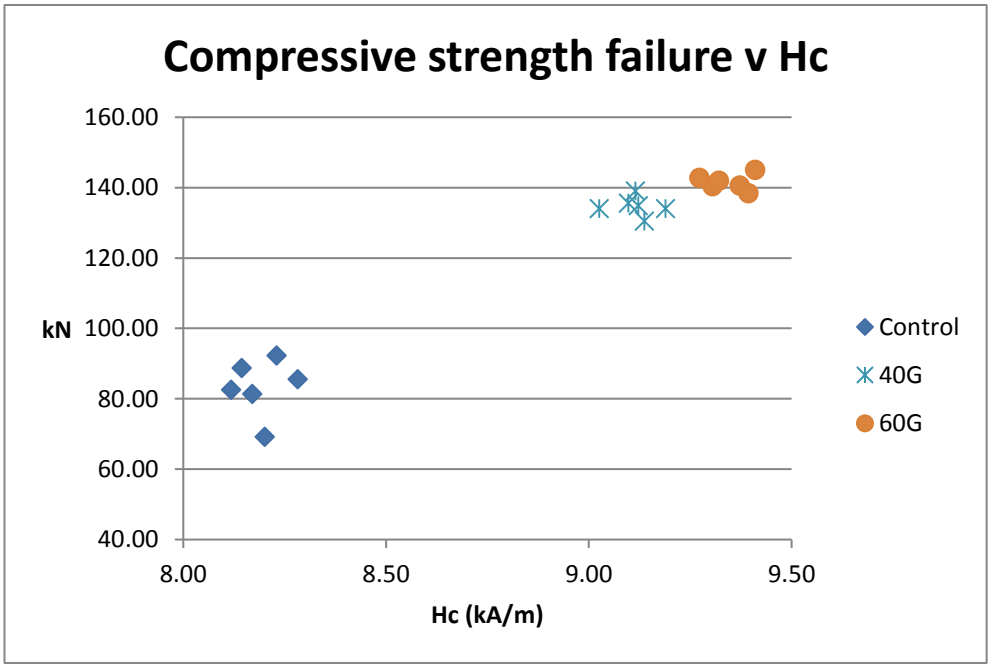

Figure 27. Compressive strength results as a function of Hc increase due to treatment with a clear reduction in scatter at higher treatment.

4.5 SEM EBSD assessing strain and grain size in relation to Hc

Sample 1 treated at 40 G was used to investigate whether it is the changes in the WC or the Co phase which contribute most to the observed increase from 8.2 KAm^{-1}

up to 9.2 KAm^{-1} in coercivity after tumbling. Analysis using ANOVA indicated that grain refinement was evident in both untreated and the treated samples, peaking at a depth of 0.2mm from surface. Since it is known that depth dependant grain refinement is a characteristic from sintering and no further grain size reduction in the treated sample was measured. It follows that the observed change in Hc must be a result of changes in the Co binder and not due to a decrease in WC grain size due to the impacts fracturing and re-embedding into the sample.

To investigate the distribution of strain in WC and CO, strain contouring from EBSD was be used, the results are shown in Figure 29.

(a)

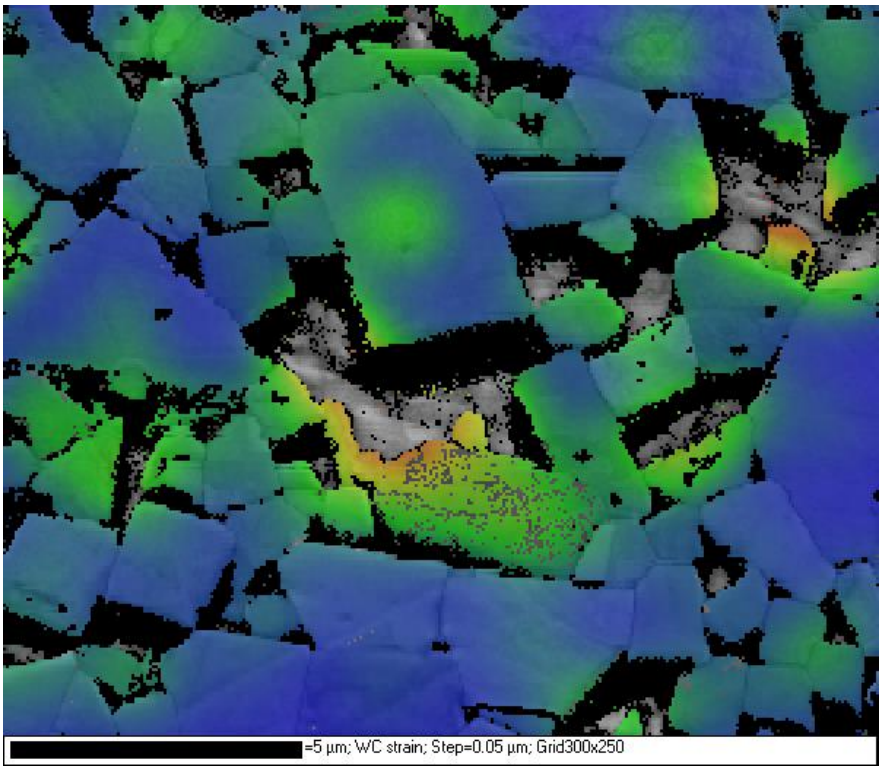

(b)

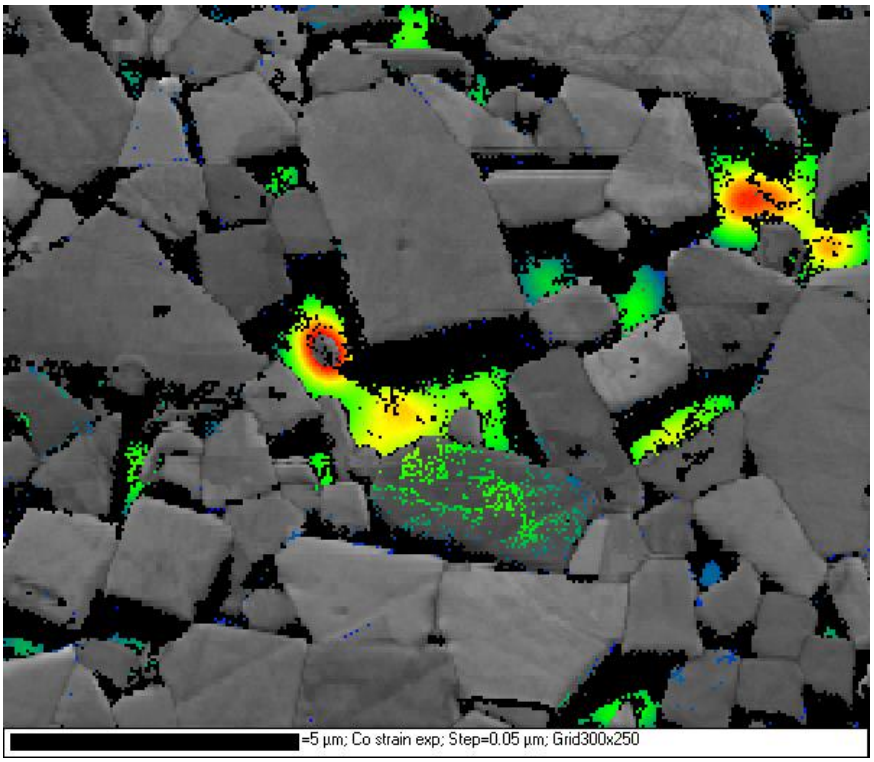

Figure 28. Strain contouring for (a) WC and (b) Co for the un-tumbled sample

The relative indexing rate of Co and the proportion of hcp/fcc were observed to vary between the samples. For Sample 1 the proportion of Co corresponds to 17 vol%, the absolute maximum index % which could be expected for Co assuming a 100% indexing rate. Indexing rates for Co from the unprocessed sample were only around 5% which can be due to the relative softness and hence lower crystal quality of the Co phase relative to WC and sample preparation. Co grain boundaries also act as scattering centres which lowers the detection rate still further. There was a marked lower detection rate for the energetically processed acoustic tumbled sample as seen in Table 13.

Table 13. Summary of Co detection from OIM mapping

Process	Depth mm	fcc	hcp	Total Co (%)	Hc
Untumbled	3	0.537	2.026	2.563	8.21
Untumbled	1	0.863	1.861	2.724	8.21
Untumbled	0.2	0.645	1.925	2.570	8.21
Untumbled	0.1	0.349	1.631	1.980	8.21
Acoustic Tumbled	3	0.124	1.375	1.499	9.2
Acoustic Tumbled	1	0.029	1.006	1.035	9.2
Acoustic Tumbled	0.2	0.028	1.286	1.314	9.2
Acoustic Tumbled	0.1	0.027	1.234	1.261	9.2

Treatment and sample depth are observed to affect the ratio with the fcc phase being less prevalent in the high-energy processed samples. Examination of the correlations between treatment and depth variables, found that depth was a much weaker predictor for Co detection than the treatment variable as summarized in Table 14.

Table 14. Summary of Co detection and sample variables.

Variables	Correlation	P value
Process: Total Co	Negative	0.0266
Total Co: Hc	Negative	0.0165
Depth: Total Co	Positive	0.06
hcp: Hc	Negative	0.0327

The observed decrease in Co detection with sample depth can be attributed to the observed WC grain refinement which results from the sintering process. A finer WC phase will lead to increased scattering from WC/Co phase boundaries relative to coarser regions and this could account for the variation attributable to depth. However from the data, it is clear that the overriding factor that affects the detectability of the Co is related to the treatment process causing increased strain in the Co phase, reducing the long-range order and therefore the ability to scatter electrons. This is

considered to be what leads to the observed drop in detectable Co from EBSD analysis. In table 14 it is clear that the fcc phase was much reduced in the treated sample, fcc detection was less than 10% of hcp throughout the depths analysed. It is plausible the treatment forces a phase change from fcc – hcp or fcc loses long range crystal order faster when lattice parameters are distorted as a result of strain. Certainly the hcp structure is more close-packed than the fcc structure and is in fact the stable structure of pure Co. The hcp phase readily forms twins, which gives it more mechanisms to absorb dislocations without disrupting the crystal lattice. If the sample was treated at higher kinetic energies then it is probable that all remaining detectable Co will be hcp. It is probable that there will be a limit to how strained the Co phase can be before Hc no longer increase with increased Co strain due. A positive correlation between depth from sample surface and grain size was observed but since this was also true for as-sintered and treated sample this was taken to be a sintering artifact and not a result of the acoustic tumbling process. Therefore, the observed change in Hc must be a result of changes in the Co binder and not the WC phase.

4.6 Transmission Electron Microscopy

Figures 30 and 31 are images of WC and Co before and after the acoustic tumbling treatment. It was taken from an area approximately 200 micrometers from the surface. The white contrast WC phase is present as discrete grains forming a network while the darker contrast Co phase forms a sparse interpenetrating network with a diffuse grain structure. The WC grains in the untreated material have a comparatively low dislocation density, with some dislocation loops observed (Figure 30). No defects or dislocations are visible in the cobalt phase, this is confirmed at closer magnification shown in Figure 32. The high density of dislocation and other defects, as shown in Figure 31, clearly shows the impact the treatment has upon the whole microstructure.

It is clear the treatment had not just an impact on the metallic phase of the system but also the α-phase.

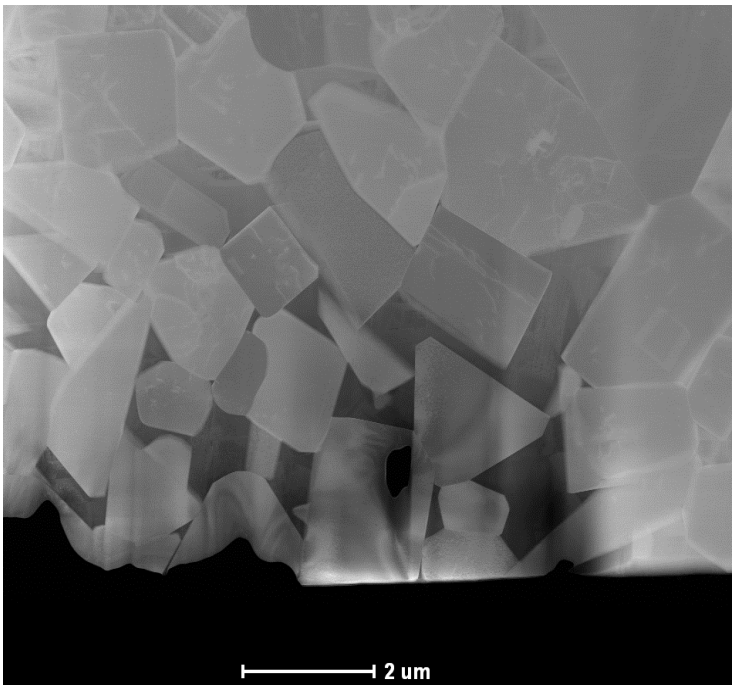

Figure 29. TEM image of WC/Co cemented carbide prior to treatment. The lighter contrast angular structures is tungsten carbide particles with the darker cobalt phase interspaced

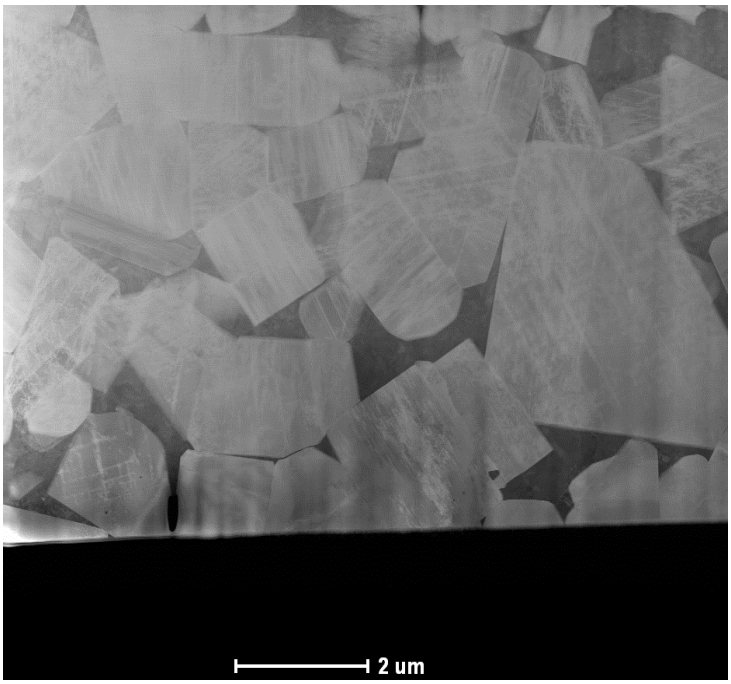

Figure 30. TEM image of WC/Co cemented carbide after treatment. Vast amount of dislocation is visible throughout the microstructure

It is known that the cobalt grains in a cemented carbide material have a dendritic morphology and can be very large [58]. The size of a single-crystallographic orientation can be up to 50 times greater than the average size of the WC grains [59]. This is evident in Figure 32 with the dark region making up a small area of one cobalt grain. The cobalt binder phase in the deformed material had however, a much reduced grain size and the dendritic morphology seemed to be lost (Figure 33) Submicron cobalt grains can also be identified. The image of the binder phase in Figure 33 helps to explain the reduced indexing information obtained from the EBSD and XRD analysis.

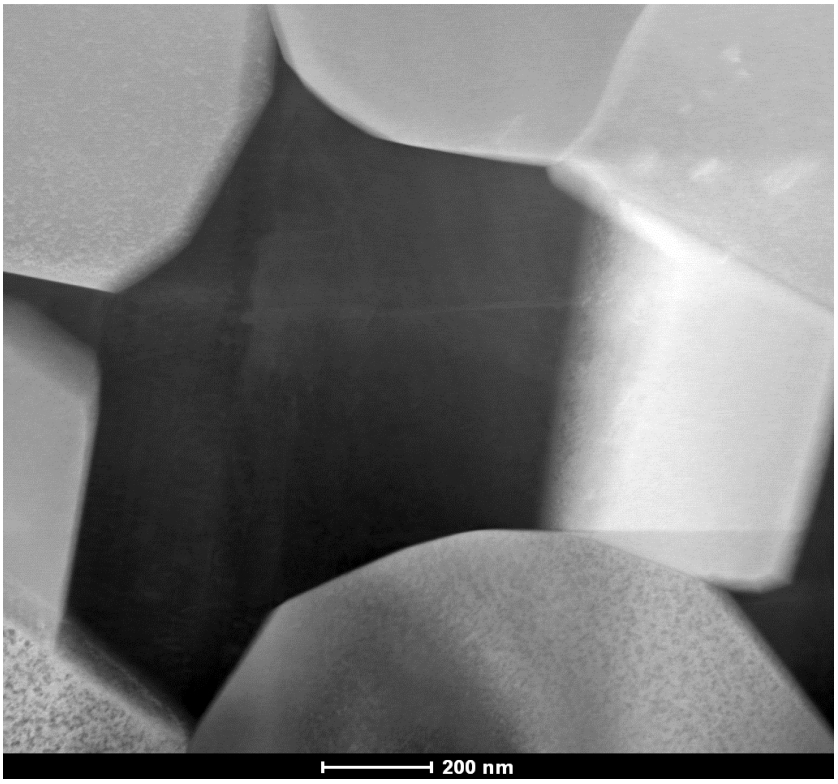

Figure 31. TEM image of sample without treatment. Faceted tungsten carbide grains are surrounding the cobalt binder.

Figure 32. TEM image of sample after treatment. The cobalt binder, surrounded by the tungsten carbide particles, appears to be highly disordered.

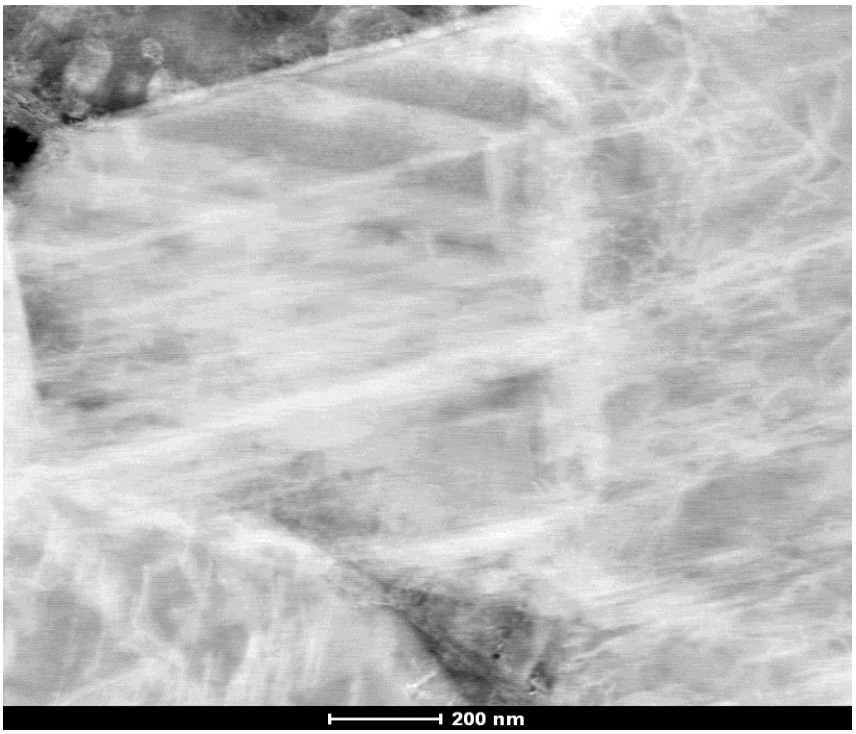

Figure 33. TEM image of sample after treatment. The fracture lines in the tungsten carbide particle is more visible at higher magnification.

The WC grains in Figure 33 and 34 are still visibly angular with no loss of morphology due to treatment except for a significantly increased number of dislocations.

4.7 XRD

The X-ray diffraction spectra collected from the untreated and treated samples are shown in Figure 35. The bottom diffraction spectrum is that of the control untreated cemented carbide sample, in which the lines for tungsten carbide and cobalt are clearly visible. In the top diffraction spectrum, the treated sample clearly shows that the peaks attributable to cobalt have almost disappeared and the tungsten carbide peaks are much broader and weaker. When considering the vast dislocations witnessed in the TEM images the strain hardening of both W and Co is clearly the cause of the shift in the spectrum.

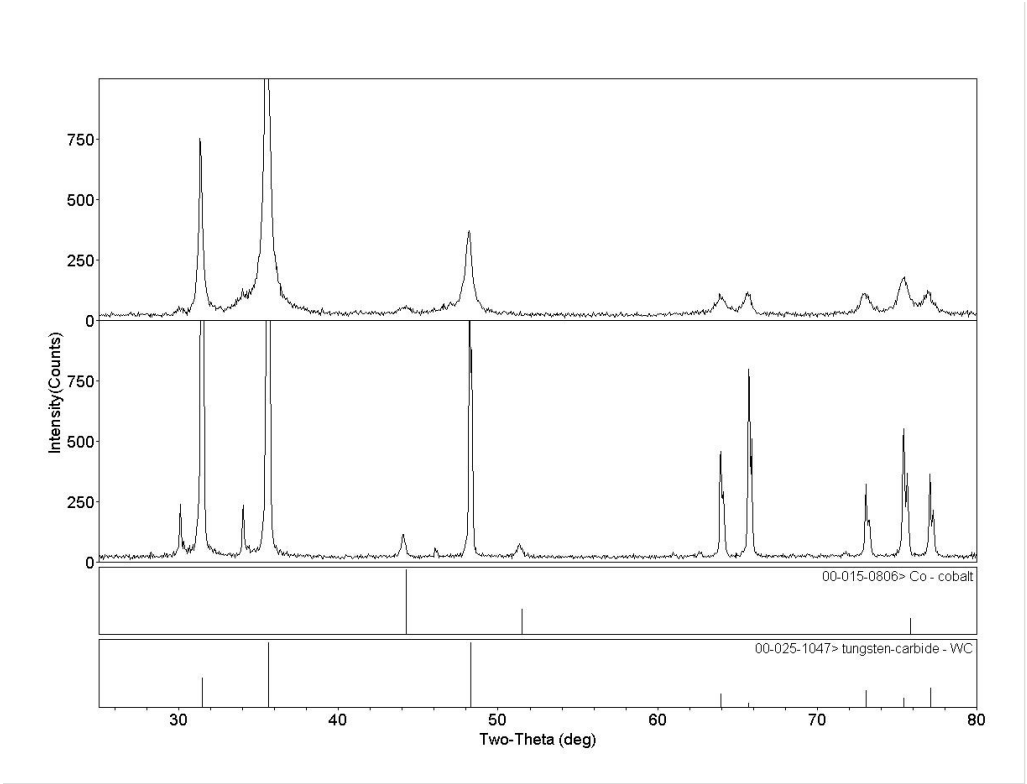

Figure 34. X-ray diffraction pattern of treated tungsten carbide (top) and standard tungsten carbide

4.8 Micropillar compressive strength tests

FESEM micrographs of two micropillars compressed up to the maximum strain of 5% are shown in Figure 36 (untreated sample) and Figure 37 (treated sample). The image obtained from the untreated sample (Figure 36) shows that two different shearing mechanisms have occurred during the compression, as shown by the black arrows. Generally, shearing does not occur exactly at the interface, but rather proceeds within the binder very close to the phase boundary and parallel to it [60, 61]. The top arrow is related to the shearing of the binder while the second one on the shearing of the WC crystal.

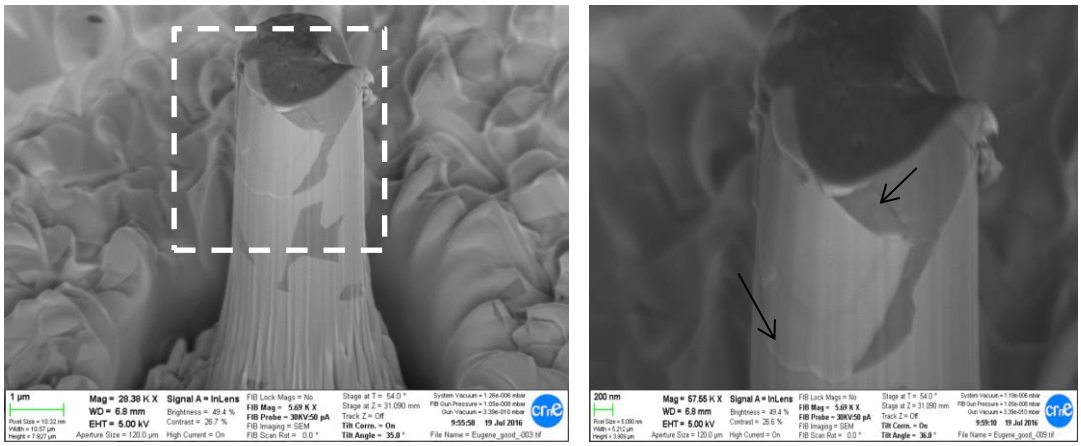

Figure 35. FESEM micrographs of compressed micropillar at 5% strain. The inset shows the appearance of the details of the micropillar after the compression. Two sheared locations have been labeled with the black arrows.

Analysis of the treated specimen (Figure 37) revealed no discernible damage at the top of the pillar, after 5% straining. The shearing mechanisms observed in the untreated samples was absent in the treated pillar. The effect of the Strain hardening on the deformation behaviour of the material is highlighted in the load-displacement curves in Figures 38.

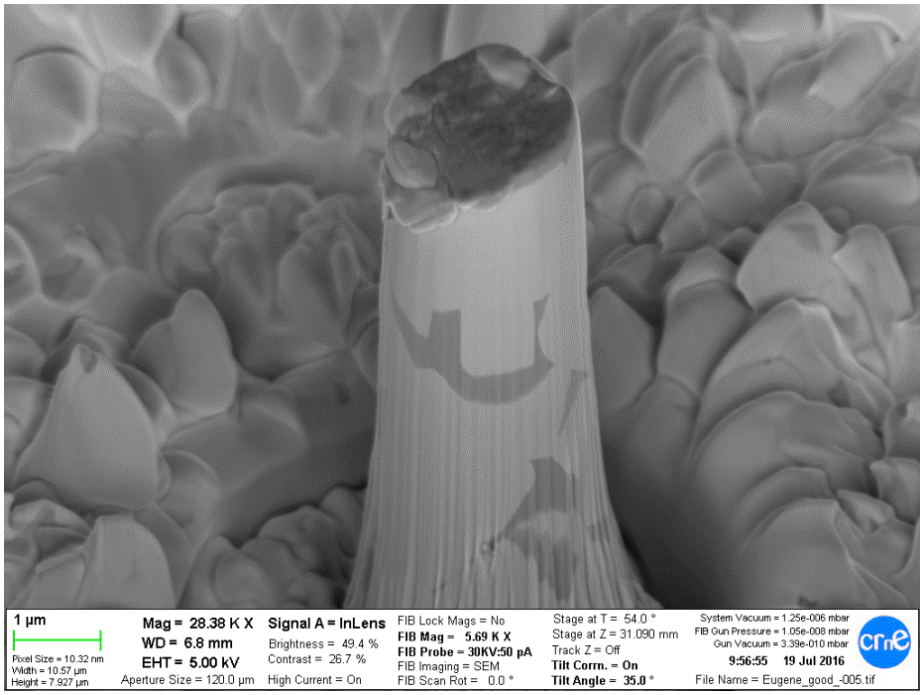

Figure 36. FESEM micrograph of micropillar with the treatment showing no observable slip traces or damages after the compression to 5% strain.

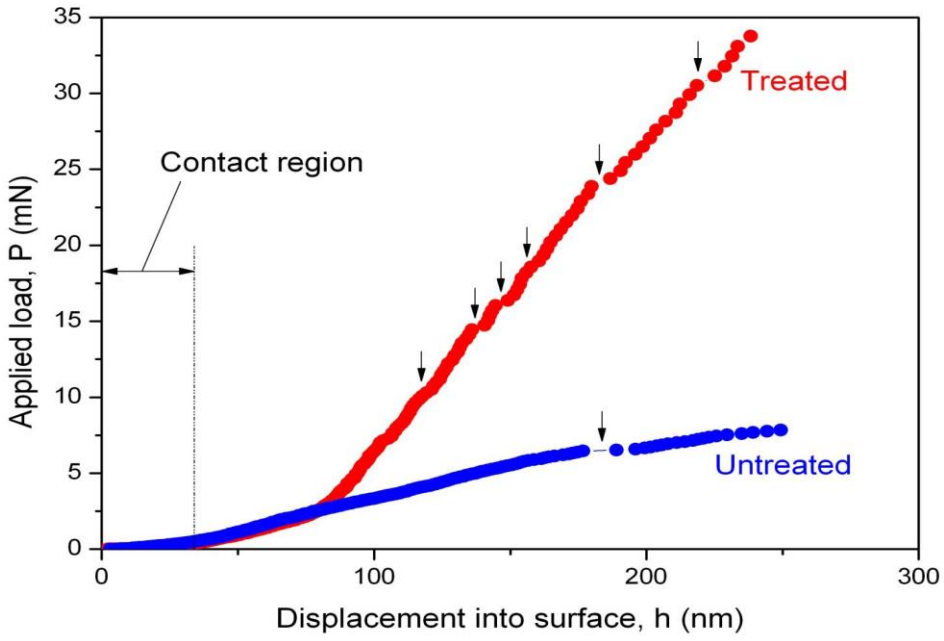

Figure 37. Load-displacement curves recorded from the compression test on the treated (red) and untreated (blue) specimens. The black arrows present different discontinuities or displacement bursts during the compression process which is likely related to the plastic flow of the material. This suggests that the flow stress recorded from the treated sample is much higher than that from the untreated sample (5 times at the 5% strain), due to the presence of the CRS.

Figure 38 presents the loading response, resulting from monotonic compression at the constant maximum strain of around 5%. As it is observed for the treated specimen, the loading curve present an obvious hardening response with small strain (displacement) bursts suggesting more homogeneous plastic flow compared with the untreated sample where only one strain burst can be observed and the sample cracked at 5% strain.

For the untreated sample, a yield stress value in the region of 2-2.5 GPa was derived. This correlates well with the findings by Tarragó et al [62]. This is much lower than the intrinsic yield stress values reported for WC phase (i.e. ~ 6-7 GPa) [63]. The flow stress at 5% strain recorded form the treated sample is about 10 GPa. In summary, the treated sample appears much harder due to the existence of the large number of dislocations as shown in the TEM images. It is clear the strain hardening due to the surface mechanical treatment makes the treated sample less prone to brittle failure.

5 Summary

5.1 Conclusions

Using a patented surface mechanical treatment developed during these investigations, the project studied the process and the effect of introducing compressive residual stress on real cemented tungsten carbide components and the consequent strain hardening of the Cobalt and WC. Microstructure and mechanical properties of the processed materials were investigated. A few conclusions can be drawn from this study:

1. The treatment method was studied and the optimum parameters for the acoustic tumbling treatment method were established. Utilizing discreet element modelling it is shown that model 1, set at 40 G acceleration, predicts the kinetic energy of the system to be in the region of 3.04± 1.28 Joules with an overall mean granular temperature that indicates the internal energy fluctuation of the particle system of 1.01± 0.042 $m^2 \cdot s^{-2}$. In model 2 the number of particles and volume of container have been adjusted to define the optimum parameters for the treatment. The results showed that the nominal height of the particle bed within the container should be considered in order to optimise the method. This is to allow for enough freedom between the particles in order to achieve sufficient acceleration before impact on each other. Another important factor revealed by the model is that both the bottom and the top of the container needs to act on the particles. If the height of the container is too large or if the solid fraction (the amount of particles) are too high it causes a dampening ef-

fect and the system cannot obtain a steady state during the treatment. Model 2a was defined as the optimum processing parameters.

2. Hardness measurements showed that exposing the sample to 40G acceleration in the acoustic tumbling process resulted in a 6 mm deep surface layer with increased hardness. The maximum hardness increase of 100 HV30 is found close to the surface. The depth of the residual stress achieved by this method is significantly larger than the standard tumbling prior art. The compressive residual stress and the work hardening in both the Co and WC contributes to the increased hardness.
3. Vickers indentations fracture toughness tests performed close to the surface of the treated sample with a 100 kg applied load failed to produce any Palmqvist cracks. In comparison, the control sample without treatment showed clear cracks at the corner of the indents with a K_{IC} measurement of 24.4 MPa $\cdot$ $m^{1/2}$. A significant increase in resistance to failure was observed after the treatments during the compression tests. An increase of 61% of the compressive strength was observed upon the treatment at 40G acceleration. 60G acceleration led to an increase of 70% of the compressive strength.
4. The coercivity of the samples increased with increased kinetic energy during the treatment. The change was observed to be directly related to the increase in the number of Weis domains due to the strain hardening within the cobalt phase. EBSD measurement confirmed that the increase in Hc was caused by the change in the Co binder but not due to a decrease in WC grain size. It was observed that the FCC phase seemed less resilient to stress than the HCP phase with respect to indexed % Co. Whether this means the energetic treatment forces a phase change from FCC to HCP remains to be clarified. It has been

noticed that the HCP phase of Co readily forms twins. The deformation twins may be more effective in accommodating the strain induced by the treatment without leaving significant residual strain in the crystal structure, compared to the randomly stored dislocations.

5. TEM observations, consistent with the XRD analysis, confirmed that a remarkable increase of dislocation density within the Co and WC phase. The high dislocation density strengthens the material. The cobalt binder phase in the treated material also has a heavily strained crystal lattice, and the original dendritic morphology seemed to have disappeared. This is consistent with the yield stress increase and contributed to the increased failure resistances. The vast amount of dislocations has also been observed in the WC phase upon the treatment.
6. Micro-pillars compression tests revealed a yield stress value in the region of 2-2.5 GPa for the untreated sample, whereas the treated sample showed strength up to 10 GPa without failure.

5.2 Future Work

Although the current study has highlighted the benefits of introducing CRS into the cemented carbides that causes in turn strain hardening of the WC and Co lattice, the detailed mechanism on the effect this has on the enhanced ductility, as shown in the micro-pillar tests, remains to be clarified. On this front, further in-depth analysis of the dislocation-mediated plasticity in the cemented carbides, particularly after the treatment, would be of interest. In-situ testing techniques could be useful to understand how the dislocations introduced in the treatment could facilitate the plastic flow of the material during the compression test.

References

[1] U Beste, S Jacobson, *Friction between a cemented carbide rock drill button and different rock types.* 11-12, December 2002, Wear, Vol. 253, pp. 1219–21.

[2] Anurag Gupta, Somnath Chattopadhyaya, Sergej Hloch, *Critical Investigation of Wear Behaviour of WC Drill Bit Buttons, Rock Mechanics and Rock Engineering*, Volume 46, Issue 1 , pp 169-177

[3] Sandvik marketing literature: http://www.hyperion.sandvik.com/en/products/cemented-carbide/mining-oil-gas

[4] Upadhyaya, Gopal S. *Cemented Tungsten Carbides: Production, Properties and Testing*, Noyes Publications, 1998, pp. 243

[5] Brookes, KJA. *World Directory and Handbook of Hardmetals and Hard Materials*, sixth ed. International Carbide Data, Hertfordshire, UK, 1996.

[6] J. Larsen-Basse, *Wear of hard-metals in rock drilling: a survey of the literature,* Powder Metallurgy, Volume 16, 1973, pp. 1–32.

[7] M. Lagerquist, *A study of the thermal fatigue crack propagation in WC-Co cemented carbide*, Powder Metallurgy, Volume 18, Issue 35, 1975, pp. 71-88

[8] W.D. Schubert, H. Neumeister, G. Kinger, B. Lux, *Hardness to toughness relationship of fine-grained WC-Co hardmetals* International Journal of Refractory Metals and Hard Materials, Volume 16, Issue 2, 1998, pp. 133-142

[9] B. Roebuck , E.G. Bennett, W.P. Byrne, M.G. Gee, *Characterization of baseline hardmetals using property maps*, NPL Report CMMT(A)172, April 1999

[10] A. Krawitz, E. Drake, *Residual stresses in cemented carbides-An overview*, International Journal Refractory Metals and Hard Materials, Volume 49, 2015, pp. 27–35

[11] D. Mari, B. Clausen, M.A.M. Bourke, K. Buss, *Measurement of residual thermal stress in WC–Co by neutron diffraction*, Int. J. Refract. Met. Hard Mater., Volume 27, 2009, pp. 282–287

[12] A. Rainey, J. Kita, *High-energy cascading of abrasive wear components*, 2003, Patent US2005053511

[13] M. R. Reese, K O. Malone, Varel international, *High Energy Treatment Of Cutter Substrates Having A Wear Resistant Layer*, 2009, Patent US2010075122

[14] W. Pfeiffer and J. Wenzel, *Shot peening of brittle materials - status and outlook*, 638-642, Materials Science Forum, Volume 638-642, 2010, pp. 799-804

[15] J Carlsson, G Stenberg, M. Rehnström , Atlas Copco Secoroc, *Drill bit for a rock drilling tool with increased toughness and method for increasing the toughness of such drill bits*, 2009, Patent US8720613 B2

[16] R.W. Cahn, *The Coming of Materials Science, Volume 5 of Pergamon Materials Series*, Elsevier, 2001, pp. 368

[17] Battelle Memorial Institute staff, *Cobalt Monograph*, 1960, Chapter 1, page 6

[18] Gopal S. Upadhyaya, *Cemented tungsten carbides Production, Properties, and Testing*, Noyes Publications, 1998, pp. 73

[19] J.J. McKetta, *Tungsten, Processing and Use, Encyclopedia of Chemical Processing and Design*, Vol. 59, 1997

[20] P. Van der Krogt, *Wolframium Wolfram Tungsten Elementymology & Elements Multidict.* Retrieved from http://elements.vanderkrogt.net/element.php?sym=W 2014/07/10

[21] Gopal S. Upadhyaya, *Cemented tungsten carbides Production, Properties, and Testing*, Noyes Publications, 1998, pp. 77

[22] H. Engqvist, *Microstructural aspects on wear of cemented carbides*, dissertation Acta Universitatis Upsaliensis. Uppsala, Sweden, 2000.

[23] Battelle Memorial Institute staff, *Cobalt Monograph*, 1960, Chapter 1, pp. 1 and 5

[24] Gopal S. Upadhyaya, *Cemented tungsten carbides Production, Properties, and Testing*, Noyes Publications, 1998, Chapter 3 page 73

[25] M. Christensen, S. Dudiy G. Wahnstrom, *First–principles simulations of metal-ceramic interface adhesion: Co/WC versus Co/Ti, Strength and Stability of interfaces in Cemented Carbides*, The American Physical Society 2002

[26] W.F. Gale, T.C. Totemeier, *Smithells Metals Reference Book,* 8th Edition, Butterworth-Heinemann, 2003

[27] L. Manlang, H. Xiaoying, D. Shitian, S. Daqin, C. Yumei, Y. Zhenmei, *Diffraction contrast study of microstructure and deformation process of WC-Co cemented carbide*, International Journal of Refractory Metals and Hard Materials 2, pp.129-132, 1983

[28] E. Gorkunov, A. Ulyanov, and A. Chulkina, *Quality inspection of sintered powder tungsten-cobalt products by magnetic technique*, Institute of Engineering Science, Russian Academy of Sciences (Urals Branch), Ekaterinburg, Russia

[29] Sandvik Hard Materials, http://www.allaboutcementedcarbide.com/03.html, 2008

[30] Swedish Standards institution and Swedish Metals Standards division, *Powder Metallurgy* 1978, pp. 104

[31] M. Zwinkels et al, Sandvik Machining Solutions, *Sintering Technology for cutting tools*, 2010 (not published)

[32] R. M. German, *Sintering theory and practice*, John Wiley & sons inc. 1996

[33] S. Haglund, *Sintering of cemented carbides – experiments and Modeling*. Royal Institute of Technology, 1998

[34] R.M. German, *Liquid Phase Sintering*, Plenum Press New York, 1985

[35] H.E. Exner and E. Artz, *Sintering processes*, in: R.W. Cahn and P. Haasan (eds.), Physical Metallurgy, Third edition, Elsevier Science Publishers, Amsterdam, 1983, 1885–1912

[36] J. Guo et al, *Formation of Co-capping during sintering of straight WC-10 wt% Co*, International Journal of Refractory Metals and Hard Materials 28 (2010) 317-323

[37] A. Rainey, J. Kita, *High-energy cascading of abrasive wear components*, 2003, Patent US2005053511

[38] Ed. N.R. Comins, J.B. Clark, *Specialty Steels and Hard Materials*, Proceedings of the International Conference on Recent Developments in Specialty Steels and Hard Materials 1982, Pergamon Press, 1982, pp 142

[39] E. P. Degarmo, J. T. Black, R. A. Kohser, *Materials and Processes in Manufacturing* (9th ed.), Wiley, 2003. pp 106

[40] H. Y. Miao, D. Demers, S. Larose, C. Perron and M. Lévesque, *Experimental study of shot peening and stress peen forming*, Journal of Materials Processing Technology, vol. 210, 2010, pp 2089-2102

[41] NDT Education Resource Center, 2001-2014, The Collaboration for NDT Education, Iowa State University, retrieved from, https://www.ndeed.org/EducationResources/CommunityCollege/MagParticle/Physics/HysteresisLoop.htm

[42] K. G. Stjernberg, *Some relations between the structure and mechanical properties of WC–TiC–Co alloy*, Powder Metallurgy, Volume 13, No. 25, 1970, pp. 1

[43] H. Fischmeister, H. E. Exner, Arch. Eisenhuttenwes., Vol. 37, 1966, pp. 499

[44] B. Roebuck, E. A. Almond, *Microstructural events preceding fracture in compression in hardmetals*, Conf. on Recent Advances in Hardmetal Production, Sept 1979, p28-1, Loughborough University of Technology, Metal Powder Report 1979

[45] R. Carey, E. D. Isaac, *Magnetic domains and techniques for their observation*, The English Universities Press limited, 1966 page 32, 34

[46] Hardmetals Compression Test, ISO 4506, International Organization for Standardization, Geneva, 1997

[47] L. Hu-Chul, *The hardness and deformation of tungsten-carbide-cobalt alloys*. PhD Thesis, Brown University (1977)

[48] B. B. He, *Two-Dimensional X-Ray Diffraction*, Hoboken, New Jersey, US: John Wiley & Sons, Inc., 2009.

[49] A. D. Krawitz, *The Use of X-ray Stress Analysis for WC-base Cermets*, Materials Science and Engineering, vol. 75, 1985 pp. 29-36.

[50] M. Carpenter, E. Keown, J. Smith, S. Geoghegan, *Method of Surface hardening*, 2012, Patent EP 2638992

[51] D.K. Shetty, I.G. Wright, P.N. Mincer, A.H. Clauer*, Indentation fracture of WC–Co cermets*, Journal of Material Science 20 (1985) 1873–1882.

[52] R.K. Viswanadham, T.S. Sun, E.F. Drake, J.A. Peck, *Quantitative fractography of WC– Co cermets by Auger spectroscopy*, Journal of Material Science 16 (1981) pp.1029–1038.

[53] D.K. Shetty, I.G. Wright, P.N. Mincer, A.H. Clauer, *Indentation fracture of WC–Co cermets*, Journal of Material Science 20 (1985) 1873–1882.

[54] Hardmetals, Palmqvist toughness test, ISO 28079, International Organization for Standardization, Geneva, 2009

[55] L.L. Shaw, H. Luo, Y Zhong, *WC-18 wt.% Co with simultaneous improvements in hardness and toughness derived from nanocrystalline powder*, Materials Science and engineering, 2012 pp. 39-48

[56] J. M. Tarragó, J.J.Roa, E. Jiménez-Piqué, E. Keown, J. Fair, L. Llanes, *Mechanical deformation of WC-Co micropillars under uniaxial compression*, International Journal of Refractory Metals and Hard Materials Volume 54, 2016, pp. 70-74

[57] J. Weidow, H.O. Andrén, *Binder phase grain size in WC–Co based cemented carbides*, Scripta Materialia, Volume 63, Issue 12, 2010, pp. 1165–1168

[58] D. L. Coates, A. D. Kravitz. *Effect of particle size on thermal residual stress in WC-Co, Material Science and Engineering*, Volume 359, Issue 1-2, pp. 338-342

[59] K.P. Mingard, B. Roebuck, J. Marshall, and G. Sweetman, *Some aspects of the structure of cobalt and nickel binder phases in hardmetals*, Acta Materialia, Volume 59, Issue 6, 2011, pp. 2277.

[60] L.S. Sigl and H.E. Exner, *Experimental study of the mechanics of fracture in WC-Co alloys, Metallurgical and Materials Transactions*, Volume 18, Issue 7, 1987, pp 1299

[61] H.F. Fischmeister, S. Schmauder, and L.S. Sigl, *Finite Element Modelling of Crack Propagation in WC-Co Hard Metals,* Materials Science and Engineering A 105/106, 1988, pp 305-311.

[62] J. M. Tarragó, J.J.Roa, E. Jiménez-Piqué, E. Keown, J. Fair, L. Llanes, *Mechanical deformation of WC-Co micropillars under uniaxial compression*, International Journal of Refractory Metals and Hard Materials Volume 54, 2016, pp. 70-74

[63] T. Csanádi, M. Bl'anda, A. Duszová, N.Q. Chinh, P. Szommer, and J. Dusza, *Deformation characteristics of WC micropillars*, Journal of the European Ceramic Society, Volume 34, Issue 15, 2014, Pages 4099–4103.